



MONASH University

Problems in Low Mass Stellar Rotation

Tanner A. Wilson

Doctor of Philosophy

A Thesis Submitted for the Degree of Doctor of Philosophy at
Monash University in 2023
School of Physics and Astronomy

Copyright notice

Insert one of the following notices.

Notice 1

©[Tanner A. Wilson](#) (2021).

The second notice certifies the appropriate use of any third-party material in the thesis. Students choosing to deposit their thesis into the restricted access section of the repository are not required to complete Notice 2.

Notice 2

©[Tanner A. Wilson](#) (2021).

I certify that I have made all reasonable efforts to secure copyright permissions for third-party content included in this thesis and have not knowingly added copyright content to my work without the owner's permission.

Abstract

The abstract should outline the main approach and findings of the thesis and must not be more than 500 words.

The Thesis Abstract is written here (and usually kept to just this page). The page is kept centered vertically so can expand into the blank space above the title too...

Declaration

This thesis is an original work of my research and contains no material which has been accepted for the award of any other degree or diploma at any university or equivalent institution and that, to the best of my knowledge and belief, this thesis contains no material previously published or written by another person, except where due reference is made in the text of the thesis.

Signature:

Print Name: Tanner A. Wilson

Date:

Thesis including published works declaration

This declaration is to be included in a ‘thesis including published works’. You must provide details of all publications included in your thesis in the section below. If you have not completed a thesis including published works.

Please ensure your thesis meets the [thesis including published works requirements](#). Some faculties vary requirements in terms of the number of papers required, status of papers and other criteria. These faculty specific requirements can also be found at the above link.

Please remove the above section and include a standard thesis declaration.

I hereby declare that this thesis contains no material which has been accepted for the award of any other degree or diploma at any university or equivalent institution and that, to the best of my knowledge and belief, this thesis contains no material previously published or written by another person, except where due reference is made in the text of the thesis.

This thesis includes (*insert number*) original papers published in peer reviewed journals and (*insert number*) submitted publications. The core theme of the thesis is (*insert theme*). The ideas, development and writing up of all the papers in the thesis were the principal responsibility of myself, the student, working within the (*insert name of academic unit*) under the supervision of (*insert name of supervisor*).

(The inclusion of co-authors reflects the fact that the work came from active collaboration between researchers and acknowledges input into team-based research.) *Remove this paragraph for theses with sole-authored work*

In the case of (*insert chapter numbers*) my contribution to the work involved the following:

(If this is a laboratory-based discipline, a paragraph outlining the assistance given during the experiments, the nature of the experiments and an attribution to the contributors could follow.)

Here should be the table!

I have / have not renumbered sections of submitted or published papers in order to generate a consistent presentation within the thesis.

Student name:

Student signature: Date:

I hereby certify that the above declaration correctly reflects the nature and extent of the student's and co-authors' contributions to this work. In instances where I am not the responsible author I have consulted with the responsible author to agree on the respective contributions of the authors.

Main Supervisor name:

Main Supervisor signature: Date:

Publications during enrolment

You may wish to list your publications arising from your research degree enrolment using the standard citation format of your academic unit. Remove this section if you do not have publications.

Journal articles:

- 1) Dong, Xingbo, Zhe Jin, and Andrew Teoh Beng Jin. "A genetic algorithm enabled similarity-based attack on cancellable biometrics." 2019 IEEE 10th International Conference on Biometrics Theory, Applications and Systems (BTAS). IEEE, 2019.
- 2) xxx

Acknowledgements

In accordance with Chapter 7.1.4 of the research degrees handbook, if you have engaged the services of a professional editor, you must provide their name and a brief description of the service rendered. If the professional editor's current or former area of academic specialisation is similar your own, this too should be stated as it may suggest to examiners that the editor's advice to the student has extended beyond guidance on English expression to affect the substance and structure of the thesis.

Free text section for you to record your acknowledgment and gratitude for the more general academic input and support such as financial support from grants and scholarships and the non-academic support you have received during the course of your enrolment. If you are a recipient of the "Australian Government Research Training Program Scholarship", you are required to include the following statement:

"This research was supported by an Australian Government Research Training Program (RTP) Scholarship."

You may also wish to acknowledge significant and substantial contribution made by others to the research, work and writing represented and/or reported in the thesis. These could include significant contributions to: the conception and design of the project; non-routine technical work; analysis and interpretation of research data; drafting significant parts of the work or critically revising it so as to contribute to the interpretation.

Contents

Copyright notice	i
Abstract	ii
Declaration	iii
Thesis including published works declaration	iv
Publications during enrolment	vi
Acknowledgements	vii
List of Figures	x
List of Tables	xiii
Abbreviations	xv
Constants	xvi
Symbols	xvii
1 Introduction	1
1.1 History of observation of rotation	2
1.2 Evolution of rotation	5
1.2.1 Birth - Terminal age main sequence	5
1.2.2 Post-main-sequence	18
1.3 Effects of rotation	30
1.3.1 Hydrostatic effects	30
1.3.2 Increased mixing in stars	31
1.3.2.1 Dynamical shear instability	33
1.3.2.2 Solberg-Høiland instability	34
1.3.2.3 Secular shear instability	34
1.3.2.4 Meridional circulation	36
1.3.2.5 Goldreich-Shubert-Fricke instability	37
1.3.3 Magneto-rotational instabilities	38
1.3.3.1 Tayler instability and the Spruit Dynamo	38
1.3.3.2 Azimuthal Magnetorotational instability	39
1.3.4 Other angular momentum transport mechanisms	40

1.3.5	Implementation of diffusive processes in models of rotating stellar evolution	41
1.3.5.1	Transport of Angular momentum	41
1.3.5.2	Transport of Elements	42
1.3.6	Stellar Winds	42
1.3.7	Summary - Effects of rotation on low-mass evolution	46
1.3.7.1	Pre-main sequence	46
1.3.7.2	Main sequence	47
1.3.7.3	Post-main sequence	48
1.4	Todo	49
2	The Intermediate Period Gap	50
2.1	Introduction	51
2.1.1	Stellar activity indicators	54
2.2	The decrease in photometric variability of stars near the intermediate period gap	56
Bibliography		66

List of Figures

- | | | |
|-----|--|----|
| 1.1 | Normalised 2D histograms of the <i>Kepler</i> (McQuillan et al., 2014) (Top), <i>Gaia</i> DR3 (Distefano et al., 2022) (Middle), and Zwicky Transient Facility (<i>ZTF</i>) (Lu et al., 2022) (Bottom) samples. Each sample probes a different area of the rotational period against colour space with some overlap. This expands our knowledge of the evolution of rotation to different types of stars while the agreement between these samples confirms their independent accuracy. | 7 |
| 1.2 | Angular rotation rate (relative to solar) distributions of low-mass young open clusters and the Sun. Triangles, inverted triangles, and squares represent the 90 th , 25 th , and median rotation rates of the cluster. Open circle denotes the present value of the rotation rate of the Sun. Median values indicate that the rotation rate of cluster is approximately constant with age, despite the spin up by accretion. In order of increasing age (left to right) the clusters are ONC (1 Myr) (Herbst et al., 2002), NGC 6530 (Henderson & Stassun, 2012), NGC 2264 (2 Myr) (Affer et al., 2013), NGC 2362 (5 Myr) (Irwin et al., 2008), h PER (13 Myr) (Moraux et al., 2013), NGC 2547 (40 Myr) (Irwin et al., 2008), Pleiades (120 Myr) (Hartman et al., 2010), M50 (130 Myr) (Irwin et al., 2009), M35 (150 Myr) (Meibom et al., 2009), M37 (550 Myr) (Hartman et al., 2009), Praesepe (578 Myr) (Delorme et al., 2011), Hyades (625 Myr) (Delorme et al., 2011), and NGC 6811 (1 Gyr) (Meibom et al., 2011). Sourced from Gallet & Bouvier (2013), Figure 1. | 9 |
| 1.3 | Scatter plot of various cluster rotational periods against effective temperature overlayed on the <i>Kepler</i> McQuillan et al. (2014) rotational period sample. The agreement between low mass Praesepe and NGC6811 periods implies mass dependent core-envelope coupling for young (<1 Gyr) stars. Sourced from Top left panel of Figure 7 in Curtis et al. (2020) | 10 |
| 1.4 | Scatter plot <i>Gaia</i> $B_P - R_P$ colour against log of the rotational period of the <i>Kepler</i> McQuillan et al. (2014) rotational period sample coloured by the log of the photometric variation (R_{var}). R_{var} decreased towards the gap from above and below, suggesting the intermediate period gap is representative of a minimum of observability of rotation period. Highlighted by arrows in this Figure are two features that we discuss in more detail in this Section: the intermediate period gap and the long-period pile-up. | 13 |

1.5	Rotation period against $Gaia B_P - R_P$ from <i>Kepler</i> , <i>ZTF</i> overlayed with various open cluster measurements. Highlighted by this Figure is the disappearance of the intermediate period gap above $B_P - R_P = 2.5$ - the fully convective star boundary. This suggests that the rotational period gap is related to the coupling of the core and surface of low mass stars ($0.4 M_{\odot} < M < 1.3 M_{\odot}$). Sourced from the top panel of Figure 8 in (Lu et al., 2022)	15
1.6	Core (red) and surface (blue) rotation rates with additional angular momentum transport following the prescription of Spada et al. (2016). Coloured sections denote evolutionary milestones and the works that have provided constraints to these milestones. Pink: subgiant core and surface rotation, Orange: red giant branch cores, Green: clump core rotation rates, and Purple: white dwarf rotation rates. Adapted from Figure 3 in Fuller et al. (2019)	21
1.7	log of core to surface rotation rate against $\log g$. Dots: Observed core to surface rotation rates of the six subgiants measured in the Deheuvels et al. (2014) sample (A,B,C,D,E,F). Lines: rotating models of the stars in that sample without additional angular momentum transport (Eggenberger et al., 2019). The observed core-to-surface rotation rates are much smaller than models predict. This implies additional angular momentum transport than is currently accounted for models. Sourced from Figure 2 in (Eggenberger et al., 2019)	23
1.8	Same as Figure 1.7 but with additional angular momentum transport introduced for the models to reflect the observations. Sourced from Figure 3 in (Eggenberger et al., 2019)	24
1.9	Average core rotation rates of red giants against mixed mode density (a proxy for evolution) Dots: Observed core rotation rates from Gehan et al. (2018) Lines: rotating models of the stars in that sample without additional angular momentum transport (Moyano et al., 2022). The observed core rates are much smaller than models predict. Implying excess angular momentum transport is required for the models to reflect the observations. Sourced from Figure 6 in (Moyano et al., 2022)	25
1.10	Same as Figure 1.9 but with additional angular momentum transport introduced for the models to reflect the observations. Sourced from Figure 7 in (Moyano et al., 2022)	26
1.11	Surface rotation period against effective temperature of subgiants in the Santos et al. (2021) sample overlayed over the <i>Kepler</i> McQuillan et al. (2014) sample. Sourced from the bottom panel of Figure 5 in (Santos et al., 2021)	28
1.12	Surface rotation period against mass of red giant stars from Ceillier et al. (2017). Sourced from the top panel of Figure 7 in (Ceillier et al., 2017)	29
1.13	Left: PMS HR diagram tracks of $1 M_{\odot}$ solar metallicity models with and without rotation. The continuous line corresponds to a non-rotating model, while the dashed line corresponds to a rotating model with $\Omega = 20\Omega_{\odot}$. The tracks end when the ZAMS is reached. Right: Surface lithium abundance with time during the PMS for the same models. Sourced from Figure 1 in Eggenberger (2013)	46

1.14 Left: MS HR diagram tracks of $1 M_{\odot}$ solar metallicity models with and without rotation. The continuous line corresponds to a non-rotating model, while the dashed line corresponds to a rotating model with ZAMS surface velocity = 50 km/s. The tracks end when the ZAMS is reached. Right: Surface helium abundance with time during the MS for the same models. Sourced from Figure 3 in Eggenberger (2013)	48
2.1 HR diagram of the closeby rotating main-sequence sample colours by photometric variability (R_{per})	57
2.2 \log_{10} of the rotation period against $GaiaB_P - R_P$ colour of the closeby rotating main-sequence sample colours by photometric variability (R_{per}). In this Figure we can see clearly see the decrease in photometric variability of stars near the gap.	57
2.3 2D binned photometric variability (R_{per}) for the slices of \log_{10} of the rotation period and colour $GaiaB_P - R_P$ used in this work. Comparing this Figure and 2.2 the alignment of the minima of photometric variability and observation of stars in the gap can be seen.	58
2.4 Median and median absolute deviation of photometric variability (R_{per}) against \log_{10} of the rotation period in bins of and colour $Gaia B_P - R_P$ (indicated in brackets). Here we have fitted a cubic spline to median R_{per} and calculated minima using the first and second derivatives of the fitted cubic spline. The minima here are shown by solid vertical blue lines. These minima align with the rotational period gap.	60
2.5 The position of the identified minima in R_{per} against rotational period using the full close-by rotating main-sequence Kepler sample, the R_{per} minima identified with the Kepler LAMOST cross-match and the $\log_{10} R_{HK}^+$ minima identified with the Kepler LAMOST cross-match.	61
2.6 Median and median absolute deviation of photometric variability (R_{per}) (blue) and $B_P - R_P$ (orange) against \log_{10} of the rotation period in bins of and $Gaia B_P - R_P$ colour (indicated in brackets). The position of the minima in R_{per} do not align with a maxima or minima in $B_P - R_P$ implying that the colour bias when fitting across the dearth can be the cause of the R_{per} minima.	62
2.7 The LAMOST chromospherically active and Kepler rotating closeby, main-sequence cross-match \log_{10} of rotational period \log_{10} against $GaiaB_P - R_P$ colour coloured by $\log_{10} R_{HK}^+$. It is unclear from this whether $\log_{10} R_{HK}^+$ decreases toward the gap like R_{per}	63
2.8 Median and median absolute deviation of photometric variability (R_{per}) (blue) and LAMOST $\log_{10} R_{HK}^+$ against \log_{10} of the rotation period in bins of and colour $Gaia B_P - R_P$ (indicated in brackets). Here we have fitted a cubic spline to median of these values in each bin and calculated minima using the first and second derivatives of the fitted cubic spline. The minima in R_{per} are shown by solid vertical blue lines while the minima in $\log_{10} R_{HK}^+$ are shown in solid vertical orange lines. These minima align with each other and the rotational period gap.	64

Write shortened figure list names.

List of Tables

Abbreviations

LAH List Abbreviations Here

Constants

Speed of Light c = $2.997\ 924\ 58 \times 10^8$ ms^{-s} (exact)

Symbols

a	distance	m
P	power	W (Js ⁻¹)
ω	angular frequency	rads ⁻¹

Chapter 1

Introduction

Humans have been captivated by the stars since the dawn of civilisation, and this fascination has driven our curiosity and drive to understand the universe around us. The history of astronomy is rich and diverse. Indigenous cultures still use the stars for navigation, seasonal calendars, and mythological stories. Since the invention of the modern telescope, some would say the birth of modern astronomy in the 16th century, to the launch of the James Webb space telescope, technology has advanced during the period that this PhD was undertaken. Our ability to observe and study the stars has grown in scale and sophistication.

Each observation that we make improves our understanding of the underlying physics of the universe. In recent years the sheer amount of data available to astronomers has increased dramatically due in part to technological advances, such as space-based observatories, which allow us to perform large sky surveys in unprecedented detail. It is clear from these studies that our models of the universe are lacking in a number of important physical processes. One of these physical processes that are particularly not well understood is the evolution of stellar rotation¹.

This introductory chapter is intended to provide context for the reader to understand the following science chapters. The introductory chapter is broken down into the following sections of increasing level of detail:

Section 1.1 provides a historical overview of the history of astronomical observation and briefly introduces the techniques used to observe the rotation of stars. Section

¹Infact a majority of models of stellar evolution completely ignore angular momentum transport

[1.2](#) reviews our current understanding of the evolution of rotation from birth, through post-main-sequence evolution, to the remnants of rotating stars. Within this Section we also describe what we call the "problems of stellar rotation" that we have attempted to address in this work. Section [1.3](#) describes the astrophysical effects of rotation on stellar evolution.

The scientific works in this thesis are motivated by the problems in stellar rotation that are described in detail in this introduction. As a result, this introduction will overlap with the introductions of the scientific works' topics and serve as a companion for readers unfamiliar with the topic.

1.1 History of observation of rotation

In this section, we look back at the history of observing stellar rotation, how observations of stellar rotation are performed, the qualitative effects of rotation on stellar rotation and some of the problems that the big-data boom of astronomy has identified. This discussion will provide the necessary background to our attempts to understand and constrain the astrophysical process that underlies these problems.

The history of observing the rotating stars began with observations of the Sun². In approximately 1610, Galileo reported evidence of sunspots and tracked their motion in his book "l'Istoria e dimostrazioni intorno alle macchie solari e loro accidenti". He interpreted the motion of stellar spots on the surface of the Sun as a result of its rotation. Adding onto this work in 1630, Christoph Scheiner found that the stellar spots had different rotational periods at the poles and the equator - measurements that agree with modern observations of the Sun. This was the first observation of latitude-dependent rotation - more commonly known as latitudinal differential rotation.

The history of observing stellar³ rotation can be traced back to the early 20th century when astronomers first discovered that some stars they observed were rotating. They came to this conclusion through spectroscopic observations ([Elvey, 1929; Struve & Elvey, 1930; Struve, 1930](#)). They found that lines in their spectra were broadened due to the Doppler effect - a technique used to this day.

²as most astronomy does

³Here we make the distinction between the Sun and other stars through the use of the terms 'solar' and 'stellar' respectively

Around this time, astrophysicists such as Eddington (Eddington, 1918, 1926, 1929), Milne (Milne, 1923), von Zeipel (von Zeipel, 1924), and others delved into the theoretical aspects of the impact of rotation on stars. To simplify their work, they identified the effects of rotation on stellar structure, energy generation, shape and luminosity. Further, rotation induces mixing in stars that can transport angular momentum as well as elements. Advances in computational capabilities allowed astronomers to study the impact of rotation on the mixing of elements within stars in greater detail. This research revealed essential results: rotation significantly impacts the mixing of matter in stars. Enhanced mixing leads to an increased lifetime on the main sequence - hydrogen-rich material is transported to the core - and can create isotope anomalies, such as changes in the isotopic ratio $^{12}\text{C}/^{13}\text{C}$, nitrogen, oxygen and lithium enhancements (Maeder & Meynet, 2000; Heger et al., 2000; Charbonnel et al., 1994). Their results underlay our modern understanding of the impacts of stellar rotation on stellar evolution.

In the following decades, technological advances allowed for more precise photometric observations of stars. This paved the way for two techniques to obtain measures of the rotation of stars - stellar spot brightness modulation periods and asteroseismology.

Like with the Sun, stars were found to exhibit stellar spots. These spots cannot be realistically tracked on the surface of stars other than the Sun. They do, however, vary the star's observed brightness. With stellar spots tied to the star's rotation, these brightness variations are periodic. Measuring the period of brightness variation is used as a proxy for the rotation period⁴ of a star. Unlike the spectroscopic technique - where the inclination angle modulates the rotation rate - the rotational periods from stellar spot brightness modulations are more accurate to the star's actual rotation rate. As a result, this technique has made several fundamental discoveries about the evolution of stellar rotation. The accurate measurement of stellar rotation provides information to more accurately model a star's internal structure, dynamics and internal angular momentum transport - both at a specific point in evolution and with evolution. For example, it was found that the rate at which a star's surface rotates slows with time (Skumanich, 1972). Resultingly, measuring the stellar rotation can provide an imprecise measure of the age of a star⁵. Recent photometric missions such as Kepler (Borucki et al., 2010; Beck et al., 2011), Zwicky Transient Facility (ZTF) (Lu et al., 2022) and Gaia

⁴It is important to note here that the rotation period - time taken for one rotation - and rotation rate - frequency of rotation - of a star are not the same quantity. They are inversely related

⁵This is a contentious claim that we will discuss further in the coming sections

(Distefano et al., 2022) have provided a wealth of data, including a sample of 200,000 stellar rotational periods from stellar spot brightness modulations. Their results form the basis of a number of the problems in stellar rotation we discuss in this thesis.

Determining the rotation period of a star from stellar spots requires intermittent photometric measurements of stars - known as long-cadence observations - over the time scale of months. On the other hand, measurements made on the order of minutes - known as short cadence observations - reveal the internal structure of stars. Like bells, stars "ring" - or, more accurately, pulsate and thus vary in brightness - at particular frequencies related to the structure of the star. By measuring those frequencies, we can infer the internal structure of a star - for example, the density-sound speed profile of the star. Rotation introduces what are known as rotational splittings to the frequency profile. Rotational splittings vary between asteroseismic modes but are a weighted average of the rotation rate dependent on the structure of the star. Unlike brightness modulations from stellar spots and spectroscopic inference of rotation rate, asteroseismology can probe the rotation profile internal to the surface of a star.

Modern observations with asteroseismology⁶ have also found that the Sun, and most post-main-sequence stars, exhibit differential rotation along the radial axis - known as radial differential rotation. Measurement of the rotation profile of post-main-sequence stars has allowed us to probe these stars' internal mixing and angular momentum transport. It is important to note, however, due to the large amount of photometric data required to perform in-depth asteroseismic inference, the number of stars it has been performed on is only on the order of 100⁷ (Li et al., 2020b,a), and the constraints that state-of-the-art data can provide are limited. We would argue that the information that asteroseismology has provided has introduced more questions than currently answered.

The study of stellar rotation continues to advance and remains at the forefront of current research.

⁶and helioseismology for the Sun

⁷at the time of writing

1.2 Evolution of rotation

1.2.1 Birth - Terminal age main sequence

Before we discuss the observed evolution of rotation along the main sequence, we will briefly reflect on the methods of observing rotation in stars, where these methods are most conducive to understanding the evolution of rotation and their limitations. The three standard techniques of observing rotation in stars can be separated into three categories: measurement of the surface rotation period from stellar brightness oscillations owing to stellar spots, spectroscopic derivation of inclination projected surface velocity from doppler broadenings, and asteroseismology of rotational splittings. We will refer to these techniques by their data products: stellar spot rotation periods, spectroscopic rotation velocities, and asteroseismic rotation rates, respectively, for brevity. The results we discuss in this Section come from the inference of rotational evolution from stellar spot rotation. This results from two factors: stellar spot rotation periods are more accurate and less data and computationally intensive than their spectroscopic and asteroseismic counterparts.

While the spectroscopic rotation velocity has been inferred for orders of magnitude greater numbers of stars, the observed rotation rate is modulated by the inclination angle of the star relative to the observer ($v \sin i$). Constraining the evolution of rotation through spectroscopic rotation velocities of stars is only fruitful with independent constraints to stellar inclination. The stellar inclination is often difficult to measure as it requires either that the star is in a binary⁸ or that the star is intensively asteroseismically studied. As a result, only a few studies of the evolution of rotation rely on this data.

On the other hand, determining the rotation rate of stars with asteroseismology is computationally and data-intensive. We will discuss the difference in computational intensity in more detail when we outline how these methods are performed. Here we will focus on the difference data intensity. Obtaining high signal-to-noise asteroseismic signals of rotation requires short-cadence observations of stars over an observation period of 4 years

⁸and that the rotation axis aligns itself with the binary orbital inclination, which may always be the case [Albrecht et al. \(2011, 2013\)](#)

(Deheuvels et al., 2014). Short-cadence data is required because the oscillation frequencies of main-sequence stars must be greater than the Nyquist frequency of the observations. In the *Kepler* field, the cross-section of stars with both short-cadence observations and those observation periods long enough to obtain a high enough SNR to perform asteroseismic inference is very limited. Further, only limited constraints can be placed on the surface rotation rate from asteroseismology during the main sequence. Main-sequence stars only express p-mode⁹ solar-like oscillations with long lifetimes, which can only probe the structure of the convective surface region. Long mode lifetimes result in wide line widths of oscillations in the power spectrum. Main-sequence stars spend the majority of their lifetime slowly rotating. This results in rotational broadenings of the oscillations rather than distinct rotational splittings. Without precise measurements of the rotational splittings for many oscillation modes, precise inference of the surface rotation rates of main-sequence stars is limited.

The inefficiency of asteroseismic inference of rotation rates along the main sequence is best exhibited in Hall et al. (2021), who observed the asteroseismic surface rotation rates of 91 main-sequence stars. Figure 2. in Hall et al. (2021) compares the stellar spot rotation period with the surface rotation period from asteroseismic inference of the rotation profile. The surface rotation periods generally agree, confirming that the surface brightness oscillation period from stellar spots is indeed the surface rotation period. However, the rotation periods obtained from asteroseismology are much less precise than their stellar spot rotation period counterparts. Despite requiring much more data, the information provided by this technique is limited compared to stellar spot brightness modulation periods.

Stellar spot rotation period measurements can be made from long-cadence data with observation periods as low as 90 days (McQuillan et al., 2014). The technique employed to determine the rotation period is much less computationally intensive than required for asteroseismic inference of rotation rates. As a result and through the combination of various photometric missions, *Kepler* (McQuillan et al., 2014; Santos et al., 2021), *K2* (Santos et al., 2021), Zwicky Transient Facility (ZTF) (Lu et al., 2022), *Gaia* DR3 (Distefano et al., 2022) We show the rotational period distribution against colour (*Gaia* DR3 $B_P - R_P$) of the *Kepler* Mcquillan Sample, *ZTF* sample and *Gaia* DR3 samples in the top, middle and bottom panels of Figure 1.1 respectively.

⁹See Section ??

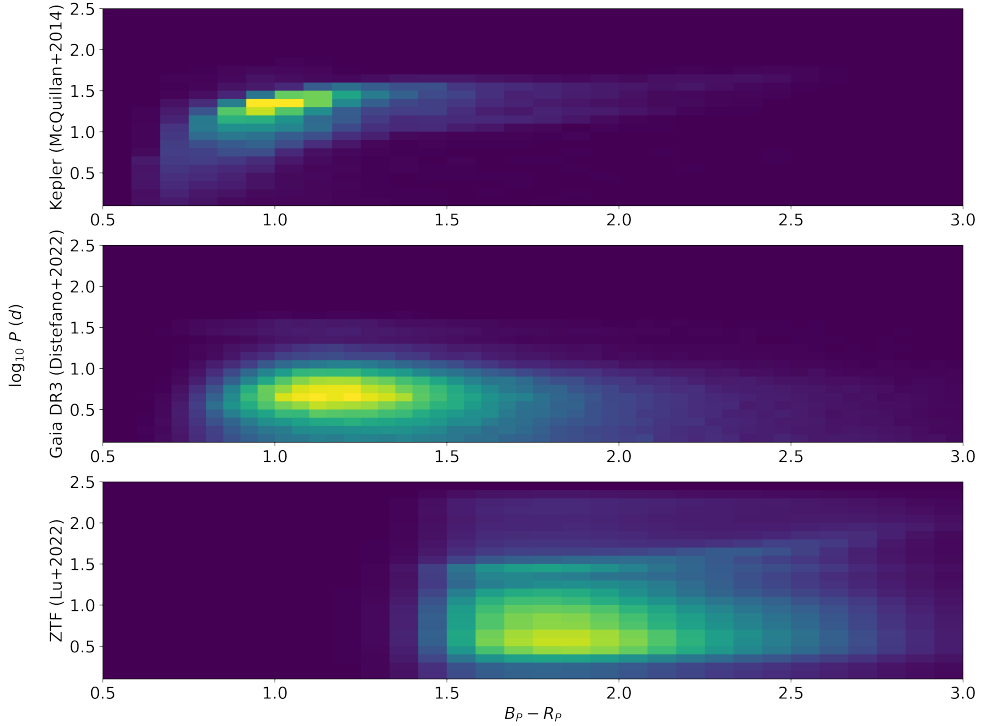


FIGURE 1.1: Normalised 2D histograms of the *Kepler* (McQuillan et al., 2014) (Top), *Gaia* DR3 (Distefano et al., 2022) (Middle), and Zwicky Transient Facility (*ZTF*) (Lu et al., 2022) (Bottom) samples. Each sample probes a different area of the rotational period against colour space with some overlap. This expands our knowledge of the evolution of rotation to different types of stars while the agreement between these samples confirms their independent accuracy.

The stellar spot rotation periods that are obtained from each of these missions are suited to observe particular masses and rotation period regimes along the main sequence. This results from the underlying telescope parameters, the scanning technique employed, and each mission’s observation cadences (Distefano et al., 2012). Comparing the rotational period distributions in Figure 1.1 we observe a few notable features and limitations from each mission. The *Gaia* DR3 rotation period sample exhibits spurious periods centred around 0.5, 18, 25, 32 and 49d. Distefano et al. (2022) suggest that the non-uniformity of the *Gaia* sampling could be the cause of these peaks. *Kepler* mainly targeted solar-like stars. As a result, in the *Kepler* sample, there is a lack of measured periods for M dwarfs and fast-rotating young stars. On the other hand, the *ZTF* and *Gaia* samples did not have this targeting bias. As a result, the *ZTF* and *Gaia* samples probe the rotation periods of the comparatively lower-mass (redder) stars. The *Gaia* DR3 rotation sample

is, as a result of the Gaia scanning law, mostly suited to detect periods of rapidly rotating stars ($P < 5$ d). Due to the long observation baseline, the *ZTF* mission was more suited to observe longer rotation periods. Combining the results of these missions, we can accurately probe the evolution of rotation along the main sequence for a wider range of stellar parameters than the individual missions permit. Further, the cross-match of stars between these missions confirm whether the individual missions themselves provide accurate measures of the stellar surface rotation period.

Most of what we know about main-sequence rotational evolution arises from measuring stellar spot rotation periods. However, the technique is limited by the requirement for stars to express stellar spots to be effective - a limitation that is invoked several times to explain phenomena discussed later in this Section. [McQuillan et al. \(2014\)](#) attempted to measure the stellar spot rotation periods of solar-like stars in the *Kepler* sample. In this work, they recovered the rotation period of 20% of stars with long cadence observations - 34000 detected rotation periods out of 133000 selected stars in the sample. On the other hand, [Distefano et al. \(2022\)](#) places the efficiency of the Gaia DR3 period detection pipeline at 0.4%. They argue that the detection efficiency is non-constant and, in fact, a function of stellar magnitude, the amplitude of the rotational modulation, the stellar rotation period and the ecliptic latitude. There may be regions of evolution where the stellar spot rotation period does not effectively probe rotational evolution.

All matter in the universe has some angular momentum. Stars are born in the core of spinning molecular clouds from the infall of matter due to gravity. As a result, all stars are rotating. The amount of angular momentum a star is born with may depend on the cloud from which it was formed.

At the beginning of the pre-main-sequence (PMS) phase, a young star is typically surrounded by a disk of gas and dust from which it is accreting material. The accretion process can lead to an increase in the rotation rate of the star, as the angular momentum of the infalling material is transferred to the star. However, as the star grows in size and mass, its magnetic field becomes stronger, which can slow down its rotation through the process of magnetic braking.

One key feature of PMS rotational evolution is the "disk-locking" phenomenon, in which the star's rotation becomes locked to the rotation of the disk ([Eggenberger et al., 2012](#)). This occurs when the star's magnetic field is strong enough to interact with the disk,

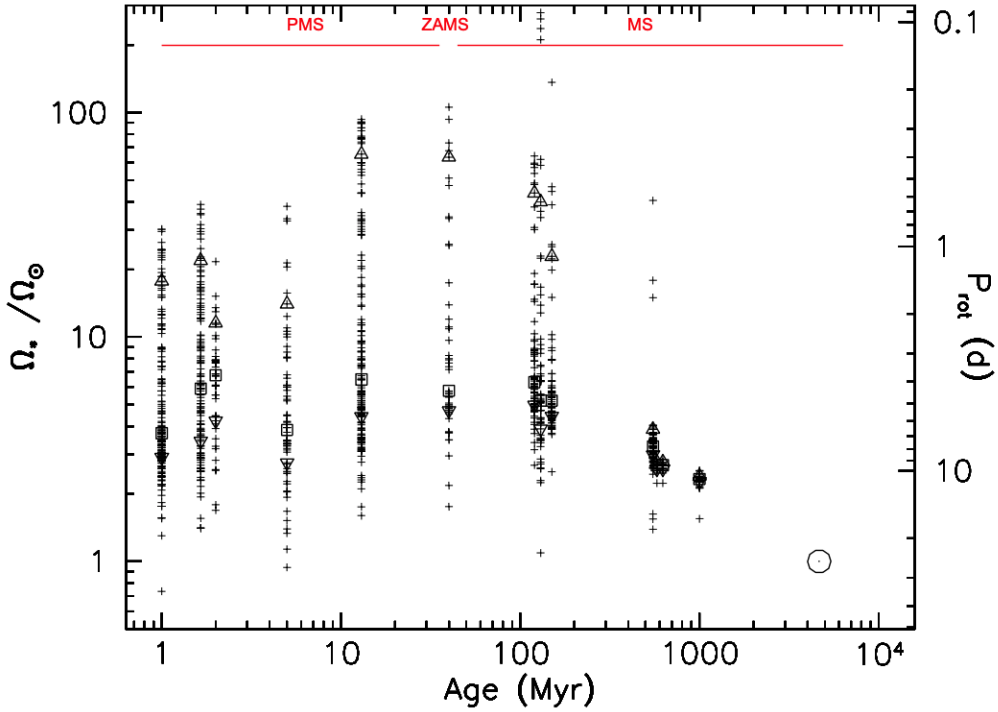


FIGURE 1.2: Angular rotation rate (relative to solar) distributions of low-mass young open clusters and the Sun. Triangles, inverted triangles, and squares represent the 90th, 25th, and median rotation rates of the cluster. Open circle denotes the present value of the rotation rate of the Sun. Median values indicate that the rotation rate of cluster is approximately constant with age, despite the spin up by accretion. In order of increasing age (left to right) the clusters are ONC (1 Myr) (Herbst et al., 2002), NGC 6530 (Henderson & Stassun, 2012), NGC 2264 (2 Myr) (Affer et al., 2013), NGC 2362 (5 Myr) (Irwin et al., 2008), h PER (13 Myr) (Moraux et al., 2013), NGC 2547 (40 Myr) (Irwin et al., 2008), Pleiades (120 Myr) (Hartman et al., 2010), M50 (130 Myr) (Irwin et al., 2009), M35 (150 Myr) (Meibom et al., 2009), M37 (550 Myr) (Hartman et al., 2009), Praesepe (578 Myr) (Delorme et al., 2011), Hyades (625 Myr) (Delorme et al., 2011), and NGC 6811 (1 Gyr) (Meibom et al., 2011). Sourced from Gallet & Bouvier (2013), Figure 1.

causing the star and disk to rotate together. Disk-locking can help to explain why some PMS stars have relatively long rotation periods, even though they are young and should be rotating rapidly due to the effects of accretion.

The interplay between accretion and magnetic braking can result in a complex evolution of the rotation rate of a young star during the PMS phase (Gallet & Bouvier, 2013). Observations of young stars in star-forming regions have revealed that the rotation rates of PMS stars span a wide range, with some stars spinning rapidly and others rotating slowly. We show this complex relationship in Figure 1.2. Comparative to the main-sequence where stars generally spin-down due to surface winds, the median rotation rate of PMS cluster is relatively constant with age.

While the many main-sequence stars have had their rotation rates measured, their ages are not well-constrained. Resultingly the evolution of rotation with age is also not well-constrained. Observations of young open clusters' main-sequence surface rotation from the *Kepler* mission suggest that angular momentum transport over a star's lifetime is consistent between clusters - the distribution of rotational periods of stars has considerable overlap between clusters (Spina et al., 2020; Curtis et al., 2020). Figure 1.3 shows the distribution of rotation rates of some open clusters. In this Figure, we can observe some significant aspects of the evolution of angular momentum in stars.

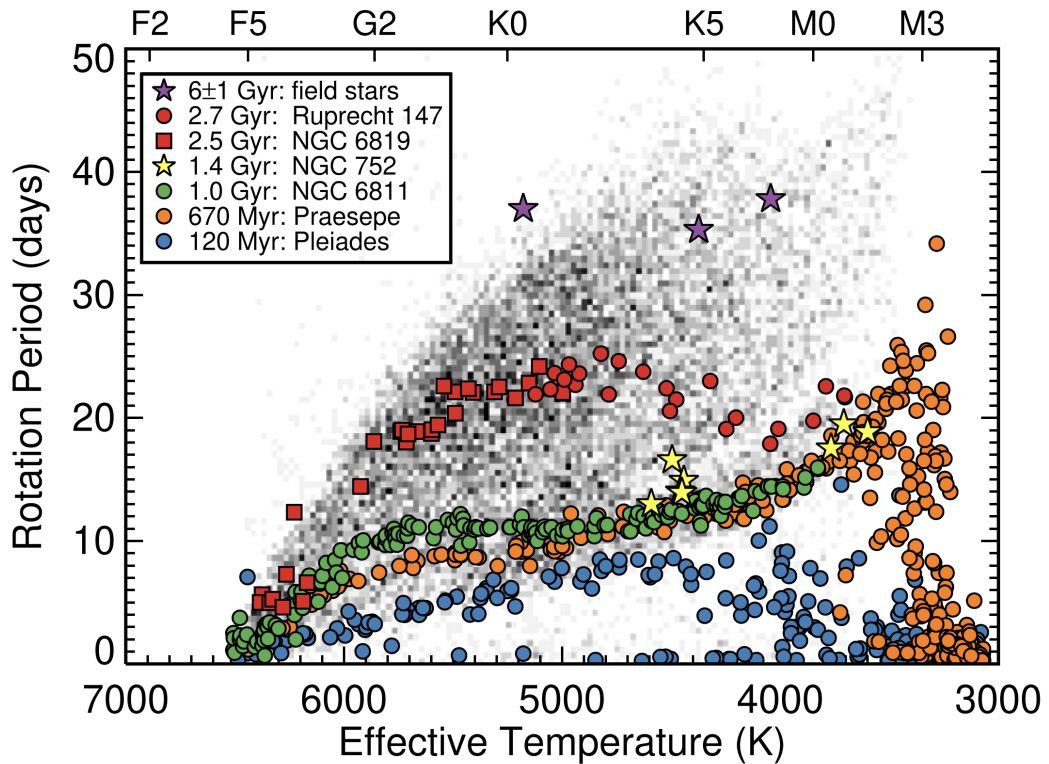


FIGURE 1.3: Scatter plot of various cluster rotational periods against effective temperature overlayed on the *Kepler* McQuillan et al. (2014) rotational period sample. The agreement between low mass Praesepe and NGC6811 periods implies mass dependent core-envelope coupling for young (<1 Gyr) stars. Sourced from Top left panel of Figure 7 in Curtis et al. (2020)

The surface rotational period increases over time for stars between $<1.1 M_{\odot}$. Within this range of masses, angular momentum is lost from the convective surface through mass loss and interactions of the star's magnetic field and the lost ionised material through stellar winds - magnetic braking. Through observations of the Pleiades, Ursa Major, and Hyades stars and the Sun, Skumanich (1972) derived the proportional relation between the rotational rate of stars and the inverse square of their age - $\omega(t) \propto t^{-1/2}$. This

proportionality forms the standard for expected rotational evolution and for what is known as gyrochronology - measuring the ages of stars from their rotational rate.

Outside the ~ 0.4 and $1.1 M_{\odot}$ range, the rotation period also decreases, albeit slower, with much more complex relationships with time. Above $\sim 1.1 M_{\odot}$, known as the Kraft break, stars have shallower convective envelopes and are believed to have less efficient magnetic dynamos - which induce strong magnetic fields. Resultingly, the magnetic braking in these stars is less efficient, and these stars continue to rotate rapidly throughout most of their main-sequence lifetimes. Below $0.4 M_{\odot}$ stars are fully convective. Angular momentum is efficiently transported throughout the star. A greater amount of angular momentum needs to be removed to slow the star's rotational rate, compared to stars that are not fully convective. The main-sequence rotational evolution of stars with mass $>1.3 M_{\odot}$ is unprobed. Above this mass, stars have no convective envelope, and thus, they do not express stellar spots nor solar-like oscillations that can be used to probe the surface rotation rate. Theoretical modelling of the rotational evolution of high-mass stars is a substantial area of research in which observations of stellar parameters such as chemical abundances must independently constrain angular momentum transport rather than observations of stellar rotation. As this work has a stronger focus on observing the rotation of stars, these results will not be discussed here. For more information, we suggest reviews of astrophysical models of high-mass stellar rotational evolution, e.g. [Heger \(1998\)](#); [Maeder & Meynet \(2000\)](#); [Maeder \(2009\)](#).

Until recently, it was assumed that there was little to no angular momentum transport between the radiative core and convective surface of main-sequence stars in the 0.4 - $1.1 M_{\odot}$ range. Helioseismic observations of the Sun suggest that only the stellar surface undergoes rotational braking, and the core remains rotating rapidly - suggesting minimal angular momentum transport between the core and the surface on the main sequence. However, open cluster rotation period observations suggest that Skaumanich-like rotational evolution alone does not explain the observed distributions of rotation periods with mass.

[Spada & Lanza \(2020\)](#) proposed that mass-dependent angular momentum transport between the core and the surface was required to explain observations of young (< 1 Gyr) open cluster rotation period distributions. In their work, they argue that clusters contain two sequences of stars: a sequence of relatively slower rotators, following the expected

coherent slowing of rotation rate following the Skaumanich relation, and a sequence of lower mass stars that appear to have a constant rotation rate between clusters of different ages. They compared the observations of the \sim 700-Myr old Praesepe and the 1-Gyr old NGC 6811 clusters. Figure 1 in [Spada & Lanzafame \(2020\)](#) compares the rotation period distribution of the Pleiades (120 Myr), Praesepe (670 Myr), and NGC 6811 (1 Gyr). Comparing observed rotation periods, they find that higher mass stars ($> 1 M_{\odot}$) that are on the slow rotator sequence of the older NGC 6811 have longer periods than their counterparts in the younger Praesepe, as Skaumanich rotational evolution suggests. On the other hand, the two clusters' rotational periods are indistinguishable at lower masses ($< 0.8 M_{\odot}$). In other words, low-mass stars have not been spinning down at all in the intervening 300 Myr. They argue that behaviour manifests mass-dependent core-envelope coupling - angular momentum transport between the core and the surface - briefly compensating for the loss of angular momentum due to wind braking at the surface. They develop a semi-analytical model of the rotational period's evolution with a star's age and mass tuned with the observations of stellar cluster rotational period distributions. This notably improves the accuracy of gyrochronology compared to the Skaumanich relation, especially for younger low-mass stars.

On the other hand the slow spin down rates of fast rotating stars could be related to saturation of the angular momentum loss due to stellar winds for fast rotating stars ([Johnstone et al., 2015a,b](#); [Gallet & Bouvier, 2013](#)). This is motivated by the saturation of magnetic field indicators for fast rotation rates - or rather low Rossby numbers ([Wright et al., 2011](#)). This could explain the slower observed spin-down of young rapidly rotating stars. Both of these prescriptions neglect each other: ([Spada & Lanzafame, 2020](#)) includes a simple stellar wind prescription that does not consider the saturated regime, while ([Gallet & Bouvier, 2013](#)) does not consider mass dependent angular momentum transport within the star.

Another phenomenon not well explained by Skaumanich-like rotational evolution is the observed intermediate period gap. [McQuillan et al. \(2014\)](#) calculated the rotation periods of 30000 stars in the *Kepler* sample from photometric oscillations of surface brightness from stellar spots. The distribution of the log of the rotational periods from this sample against their colour is shown in Figure 1.4. Following increasing rotation period as a proxy for time, this Figure highlights the overabundance of observations

followed, temporally, by a dearth of observations of particular rotational periods - the position of which varies with mass.

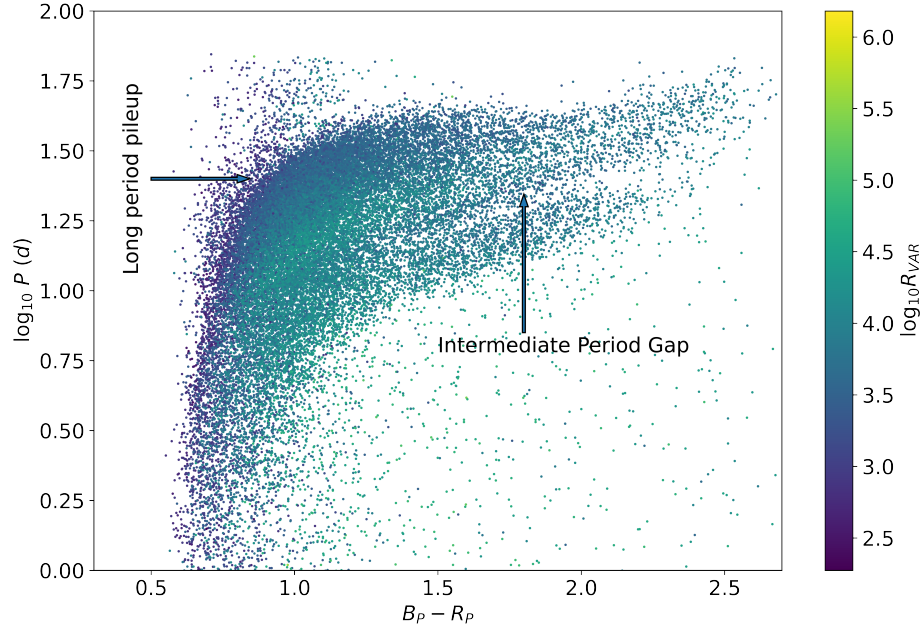


FIGURE 1.4: Scatter plot $Gaia B_P - R_P$ colour against log of the rotational period of the Kepler [McQuillan et al. \(2014\)](#) rotational period sample coloured by the log of the photometric variation (R_{var}). R_{var} decreased towards the gap from above and below, suggesting the intermediate period gap is representative of a minimum of observability of rotation period. Highlighted by arrows in this Figure are two features that we discuss in more detail in this Section: the intermediate period gap and the long-period pile-up.

Since identifying the gap, several explanations have been presented for this phenomenon. [McQuillan et al. \(2014\)](#); [Davenport \(2017\)](#) first proposed that rather than the gap being the result of modified angular momentum transport, the gap is the artifact of a recent period of bursty star formation in the *Kepler* field - resulting in a young (< 50 Myr), fast rotating, population and older, background slowly rotating, population. [Davenport \(2017\)](#) further find that the fast and slow rotators in his sample also exhibit a different distribution of the proper motion. Two kinematically separate groups favour the explanation of two epochs of star formation in the *Kepler* field. This explanation is further supported by the work of [Davenport & Covey \(2018\)](#), who showed that the gap appears to correlate with Galactic height, which is assumed to be related to stellar age.

The recent bursty star formation hypothesis accounts for the overpopulation of observations below the gap. In contrast, the dearth of observations represents the background

observation rate of rotational periods within this period range. [Gordon et al. \(2021\)](#) provided evidence against this hypothesis through analysis of *K2* data. They found that the intermediate period gap is present in the multiple pointings of the *K2* mission - suggesting that recent bursty star formation is isotropic - and that clusters with different ages contain stars that have crossed the gap.

The former suggests that all clusters universally went through a period of bursty star formation \sim 50 Myr ago. [Angus et al. \(2020\)](#) observed that the velocity dispersions of stars increase smoothly across the gap. Given that the two populations - above and below the gap - do not substantially differ in other spectroscopic and photometric observations, this scenario remains theoretically possible but unlikely. The latter requires slightly more thought. Comparing Figures 1.3 and of 1.4, the gap has a sharper slope than the sequences associated with constant age populations from Praesepe ([Douglas et al., 2017, 2019](#)), NGC 6811 ([Curtis et al., 2019](#)) and Ruprecht 147 ([Curtis et al., 2020](#)). If the bimodal star formation scenario explained the gap, the gap should have the same shape and position for each cluster and the entire *K2/Kepler* sample.

Before exploring possible explanations for the intermediate period gap, it is worth identifying where the rotational period gap occurs in the stars' evolution. [Reinhold et al. \(2019\)](#) first suggested that the gap aligns with a rotational isochrone at \sim 800Myr. With [Spada et al. \(2016\)](#) modifications to Skaumanich spin down for low-mass star to reflect the rotational distribution of clusters of known age, updated the proposed age to 750 Myr ([Reinhold et al., 2019](#)). Contrary to the hypothesis that the gap aligns itself with a certain isochrone, [Curtis et al. \(2020\)](#) identified that the open cluster Ruprecht 147 contains stars above and below the gap - as well as one star that appeared to be within the gap. This suggests that the gap does not align itself with a particular age. Instead, they argued that the gap aligns itself with a line of constant Rossby number¹⁰ = 0.5. The Rossby number is associated with the magnetic dynamo, e.g. [Noyes et al. \(1984\)](#); [Montesinos et al. \(2001\)](#); [Augustson et al. \(2019\)](#). To simplify, a star can be thought of as a volume of charged particles. As a star rotates, so do the charged particles within it. Moving charged particles induce a magnetic field - creating a magnetic dynamo. As the star rotationally evolves, so does the magnetic dynamo.

¹⁰Defined as the ratio of the rotational period to the convective turnover timescale ($Ro = P_{rot}/\tau_{conv}$) - which itself is dependent on mass and is approximately constant for a star's main-sequence lifetime

Given that the gap appears to line up with a line of constant Rossby number, this may suggest that the gap is instead caused by an event in the evolution of the magnetic dynamo rather than an event in time. This is a notable result because the magnetic dynamo is associated with a number of stellar phenomena - such as magnetorotational instabilities (angular momentum transport processes associated with the magnetic field) or stellar spots.

Other prospective hypotheses for the intermediate period gap can be broken down into two categories: (1) modified angular momentum transport and (2) decreased observability of rotation periods.

Let us consider the first hypothesis: the gap results from modifications to angular momentum transport. [Lu et al. \(2022\)](#) have shown that the gap is most apparent for stars less massive than $1.3 M_{\odot}$ and more massive than $0.4 M_{\odot}$. If we look closely at Figure 1.5 we can see that for the ZTF sample (black dots) the intermediate period gap is most apparent for stars $1.5 < B_P - R_P < 2.5$ and closes for low mass ($B_P - R_P > 2.5$) stars. Stars redder than $B_P - R_P > 2.5$ are fully convective ([Amard et al., 2019](#)), suggesting that the gap may be another phenomenon related to the interplay between angular momentum transport between the radiative core and convective surface and surface rotational braking along the main sequence.

[McQuillan et al. \(2014\)](#) first proposed that the gap is the result of two variations to Skaumanich rotational evolution. First, stars below the gap undergo a period of stalled spindown, resulting in the observed overdensity of stars along the lower branch, followed by a period of accelerated spindown, resulting in the dearth of stars in the gap¹¹.

The proposed mechanism underlying this scenario is the mass-dependent decoupling and recoupling of the core and the envelope proposed in [Lanzafame & Spada \(2015\)](#) and [Spada & Lanzafame \(2020\)](#), discussed earlier in this work. [Angus et al. \(2020\)](#) suggest that the core envelope decoupling and recoupling may explain the period gap as a break between a "younger" pile-up regime ($\text{Ro} < 0.6$) in which surface rotation periods are relatively constant with time from core-surface angular momentum transport and increase with decreasing mass from an "older" ($\text{Ro} > 0.6$) regime with the gap representing a period of relatively fast spin evolution during the transition between the two. Proponents

¹¹The authors disfavoured the hypothesis favouring the bimodal star formation hypothesis discussed earlier in this work.

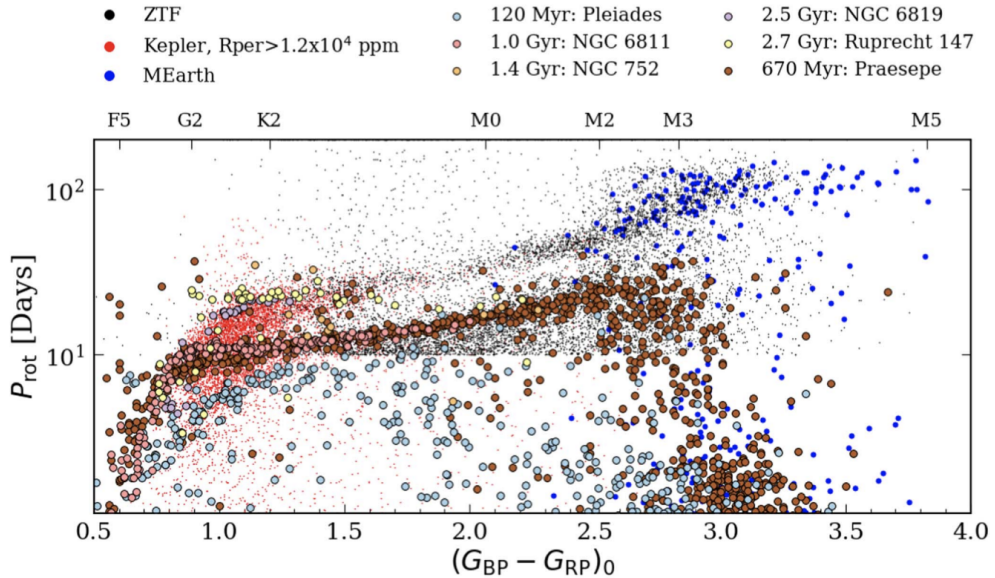


FIGURE 1.5: Rotation period against $Gaia B_P - R_P$ from *Kepler*, *ZTF* overlayed with various open cluster measurements. Highlighted by this Figure is the disappearance of the intermediate period gap above $B_P - R_P = 2.5$ - the fully convective star boundary. This suggests that the rotational period gap is related to the coupling of the core and surface of low mass stars ($0.4 M_\odot < M < 1.3 M_\odot$). Sourced from the top panel of Figure 8 in (Lu et al., 2022).

of this hypothesis suggest that the gap results from a period of enhanced spindown following core and surface recoupling where stars "jump" the gap before resuming Skumanich spindown, as is observed for older clusters. Models of - and physical mechanisms underlying - rotational evolution that reflect the proposed rapid spindown are yet to be identified. Under this model, the gap reflects an under the density of stars but would not be empty. There should be a small number of stars with $Ro \approx 0.6$, irrespective of our ability to measure their rotational periods. Curtis et al. (2020) found five Ruprecht 147 stars in or just beneath the gap yet to be thoroughly investigated.

Now let us discuss the second hypothesis: the gap results from a lack of observations of rotational periods. The rotational period of *Kepler* stars requires that stars express photometric oscillations from stellar spots. Starspots are regions of intense magnetic activity on a star's surface from magnetic flux tubes in the convection zone. These flux tubes are thought to be stretched and curled by the differential rotation of the convective region. As a result, convection is inhibited, limiting plasma flow to the surface in these tubes. This results in lower-temperature material within the tube, which looks like a darker spot on the star's surface. Stellar spots have bright perimeters surrounding the cooler internal regions of spots, known as faculae.

Stellar spots can both increase or decrease stars' bolometric luminosity. Reinhold & Reiners (2013) and Reinhold et al. (2019) propose that the gap represents the transition in stellar spot structure from spot to faculae dominance in the photosphere. Following their explanation, the gap corresponds to a transition where the increase in bolometric luminosity from the faculae negates the decrease from the internal, cooler region of the stellar spots. In the McQuillan et al. (2014) sample, stellar rotational periods are measured from the period of brightness variability due to the brightness variability introduced by stellar spots¹². Suppose the bolometric flux does not vary due to stellar spots in the gap region. In that case, the amplitude of periodic variability would decrease within this region. Reinhold et al. (2019) suggests that the gap is full of stars and represents a minimum in the detectability of rotation periods.

Supporting this hypothesis, in both the *Kepler* and *K2* fields, the variability amplitude (R_{var}) decreases towards the gap from both lower and higher rotational periods. This can be seen in Figure 1.4, which is coloured by the log of R_{var} . On the other hand, while there is evidence that stars undergo spot-to-faculae dominance, e.g. the Vaughan-Preston gap (Vaughan & Preston, 1980), this occurs much later in a star's lifetime at $Ro \sim 1$. Further, there is evidence that stars above and below the gap are both spot-dominated (Lockwood et al., 2007; Reinhold et al., 2019). Reinhold et al. (2019) speculate that activity cycles that vary the spot-to-faculae brightness contributions on rotational timescales could be the process underlying the rotational period gap. As of writing, there is no evidence to support this hypothesis.

Recent works have attempted to identify the fractional spot coverage of cluster members from their spectra (Cao & Pinsonneault, 2022). They do this by assuming the spectra of stars can be broken down into spot and ambient components that vary in temperature but are consistent in other stellar parameters. They find that the fractional spot coverage of stars is related to the Rossby number. Within this work, they observe a population of spot-coverage-enhanced stars that deviate from the relations they present.

In a follow-up work (Cao et al., 2023) they combine the angular momentum transport and decreased observation hypothesis by proposing that star spot measurements in the Praesepe open cluster are strongly enhanced only for stars that depart Skumanich rotational evolution. They suggest that a decoupling of the core and the surface explain

¹²this technique is discussed in more detail in Section ??

both observations. In their model, angular momentum transport between the core and the surface slows the increase of the rotational period. The resultant shears enhance the magnetic dynamo and, thus, stellar spot activity. Stars enhanced in stellar spot coverage are expected to have decreased observed effective temperatures. Spot-dominated, as opposed to faculae-dominated, stellar spots are cooler than the ambient temperature of the star. As a result, stars with enhanced stellar spot coverage have a decreased observed effective temperature. They then speculate that the rotational period gap is thus the result of a bias in observed effective temperature rather than a lack of observations of the rotational periods of stars in the gap.

Observations of open cluster rotational distributions beyond the gap suggest that stars $< 1M_{\odot}$ that have crossed the gap ($\text{Ro} > 0.6$) continue to spin down and follow the Skumanich-like rotational evolution until they leave the main sequence. On the other hand, there is an apparent overabundance of stars at critical rotation periods (dependent on their mass). Above this is a lack of observations of rotation periods for stars $> 5500\text{K}$. Stars with higher masses also appear to have lower rotation periods on the pile-up than their less massive counterparts. This results in what is known as the long-period pile-up, as noted in Figure 1.4. The long-period pile-up aligns itself in the [McQuillan et al. \(2014\)](#) period distribution with Rossby number ($\text{Ro} = 2.08$) ([van Saders et al., 2019](#)).

[van Saders et al. \(2019\)](#) suggest that the long-period pile-up could result from decreased magnetic braking or a lack of observations of stars beyond this Rossby number. Under the former scenario, stars stop spinning down when they reach this Rossby number as a result of weakened magnetic braking. This results in the overdensity of stars and a lack of observations of larger rotational periods. In the latter, they propose that the error in observed periods can smooth out the overdensity of stars and, in fact the lack of rotational periods is because of variations to the stellar spot activity (See above discussion of speculative explanations for decreased observation of rotational periods within the rotational period gap). Further supporting this explanation [David et al. \(2022\)](#) found that photometric variability decreases above the gap. Suggesting an unobserved population of stars with longer rotation periods.

Under the weakened magnetic braking model [David et al. \(2022\)](#) suggest that stars in this temperature regime $1M_{\odot} < M < 1.3M_{\odot}$ may spend half of their main-sequence lifetimes at the long period pile-up with only modest variances to their rotational period.

Below this mass regime, stars appear to continue to lose angular momentum through wind braking following the Skumanich relation. This results in stars with large rotational periods when they enter the post-main-sequence.

1.2.2 Post-main-sequence

For low mass ($1.1 - 1.5 M_{\odot}$) stars during the post-main-sequence, the information provided to angular momentum transport by each star can be greater than during the main sequence. While surface rotation rate can still be measured through stellar spot photometric oscillations, within this regime, the core and surface can also be simultaneously constrained through asteroseismology (at different points in evolution). This results from a combination of the expression of mixed modes, shorter mode lifetimes, and increased core rotation rates. During the main sequence, g-modes are trapped within the radiative core and thus do not introduce brightness variations (oscillations) to the stellar surface. Some g-modes can couple with p-modes in the surface convective cavity during the post-main-sequence and are known as "mixed modes". The rotational splittings of the mixed modes allow us to infer the rotation rate in the radiative region and deep core. ([Metcalfe et al., 2010](#); [Bedding et al., 2011](#)) Where, precisely, the mixed modes probe is dependent on where in the post-main-sequence the star is observed. For example, sub-giant stars express p-modes and mixed modes that can probe both the core and the surface, whereas red giant branch (RGB) stars mainly express mixed modes that can only probe the star's core. While stellar spot surface rotation periods can be measured for post-main-sequence stars [McQuillan et al. \(2014\)](#); [Ceillier et al. \(2017\)](#), asteroseismic inference of core and surface rates is the standard for probing rotation evolution in this evolutionary regime ([Deheuvels et al., 2014](#); [Gehan et al., 2018](#); [Deheuvels et al., 2020](#); [Fellay et al., 2021](#)).

Measuring the core and surface rotation rates simultaneously provides much more information to angular momentum transport than either of these quantities alone. For example, during the main-sequence, the over-abundance of stars along the lower branch of the Kepler rotation period gap could simultaneously be explained by diminished wind braking for the surface or by core-envelope recoupling. Measuring the core rotation rates would break this degeneracy. This asteroseismic quirk is useful as it allows us to directly investigate angular momentum transport more efficiently.

However, the constraints to the rotation profile of stars by asteroseismology, even in the post-main sequence, are limited. Indeed the core and surface rotation rates of subgiants can simultaneously be probed. However, where in a star the rotation can be probed depends on the observed oscillation modes, which depend on the stellar structure. The rotation rates obtained by asteroseismology are kernel-based averages of the rotation profile in regions that the observed oscillation modes probe. For example, subgiants' core and surface rotation rates are the kernel-based average rotation rates of the innermost $r/R \leq 0.05$ and outermost $r/R > 0.9$ regions (on average). Between these regions, the rotation profile is not constrained. As a result, the shape of the rotation profile, which can be fingerprints of specific angular momentum transport mechanisms at play, is also not constrained.

Asteroseismic inference of rotation rates can also be imprecise. This can be seen when comparing the surface rotation periods from asteroseismology and stellar spot photometric oscillations in [Hall et al. \(2021\)](#). This is because: a) state-of-the-art measurements of rotational splittings - the quantity that constrains the rotation profile - are low SNR and are often also imprecise, and b) the observed rotational splittings are a finite subset of the infinite number of rotational splittings that would be required to accurately and precisely constrain the entire rotation profile. With these limitations in mind, we now discuss the observed evolution of rotation of post-main-sequence stars.

Following the main-sequence, low-mass stellar rotation varies with the evolutionary phase. Models of rotating stellar evolution (e.g.)([Maeder & Meynet, 2000](#); ?) predict the following qualitative evolutionary pathway. Towards the end of the main sequence the rotation profile is largely flat. Assuming conservation of angular momentum as hydrogen core burning stops, pressure in the core drops, resulting in core contraction while the convective surface region expands. Resultingly the core is spun-up while the surface is spun-down. The core should continue to spin down as the core contracts along the RGB until entering the red clump (low-mass core He burning). The core burning reintroduces core pressure, and the resulting expansion of the core decreases the core rotation rate. When core He burning ceases, the core pressure drops again, resulting in a spun-up white dwarf (relative to the core rotation rate of red clump stars). We highlight the qualitative rotation evolution of post-main-sequence stars in Figure 1.6. Observations suggest that low-mass stars follow this pathway ([Mosser et al., 2012](#); [Deheuvels et al., 2014, 2015](#); [Hermes et al., 2017](#); [Gehan et al., 2018](#); [Deheuvels et al., 2020](#)).

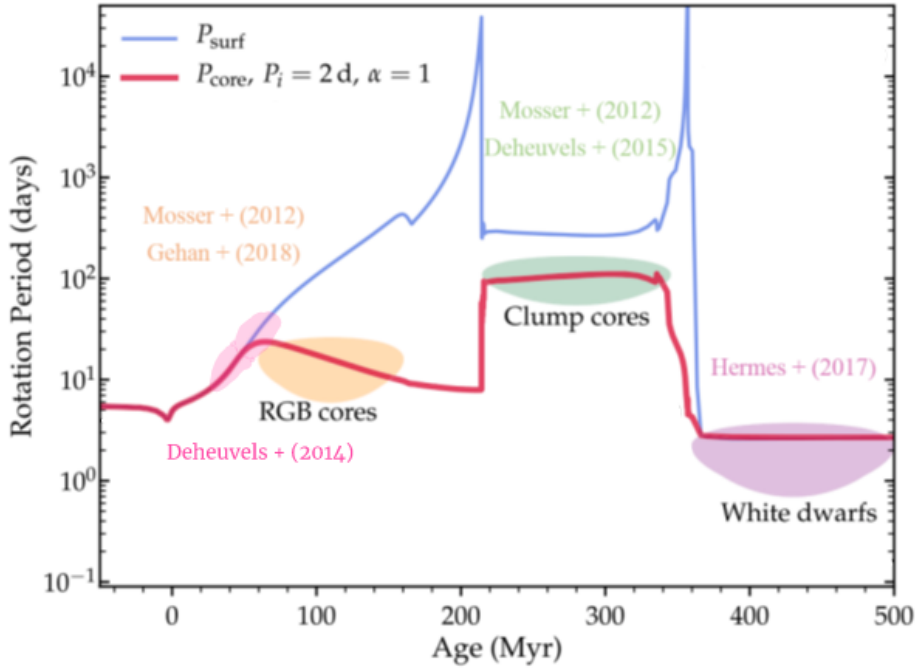


FIGURE 1.6: Core (red) and surface (blue) rotation rates with additional angular momentum transport following the prescription of Spada et al. (2016). Coloured sections denote evolutionary milestones and the works that have provided constraints to these milestones. **Pink:** subgiant core and surface rotation, **Orange:** red giant branch cores, **Green:** clump core rotation rates, and **Purple:** white dwarf rotation rates. Adapted from Figure 3 in Fuller et al. (2019)

Measuring the core and the surface rotation rates of post-main-sequence stars allows us to place constraints on the radial differential rotation of stellar interiors and quantitatively probe the evolution of angular momentum transport. Observations of young subgiants suggest that terminal age main sequence stars' rotation profiles are relatively flat (Deheuvels et al., 2020). However, observations of older post-main-sequence stars have raised more questions than they have answered (Beck et al., 2012). To summarise: angular momentum transport during the post-main-sequence must be greater than state-of-the-art models currently predict.

Deheuvels et al. (2014) measured the core and surface rotation rates of 6 subgiants/young red giants. The observed core to surface rotation ratio of subgiants and the core rotation rates of red giant branch stars suggest that additional angular momentum transport is unaccounted for in state-of-the-art models of rotating stellar evolution (Deheuvels et al., 2014; Spada et al., 2016; Moyano et al., 2022). The scale of the core-to-surface rotation rate ratio of subgiants ($\Omega_c/\Omega_{\text{surface}}$) is one to two orders of magnitude smaller than models predict (Fuller et al., 2015; Spada et al., 2016; Ouazzani et al., 2018; Eggenberger

(et al., 2019). While core rotation rates were first believed to decrease along the red giant branch¹³ (Mosser et al., 2012) revised measurements and a larger sample size revealed that the core rotation rates of red giant branch stars appear constant with evolution when the contraction of the core should spin them up. (Mosser et al., 2012; Gehan et al., 2018; Moyano et al., 2022). The core rotation rates of early red giant branch and red clump stars suggest a continued excess angular momentum transport during this phase of evolution (Cantiello et al., 2014; Moyano et al., 2022). On the other hand, observed white dwarf rotation rates can be recovered from the observed core rotation of clump stars assuming conservation of angular momentum. (Cantiello et al., 2014; den Hartogh et al., 2019) Cantiello et al. (2014) suggests that this feature may be owing to the short evolutionary timescale between the red clump and white dwarf phases rather than indicative of a decrease in the excess angular momentum transport.

The physical mechanism underlying the excess angular momentum transport is currently unidentified. Several notable relations with mass and evolutionary state have been determined by calculating the excess angular momentum transport required to match observations. Spada et al. (2016) quantified the increased angular momentum transport required to match the observed subgiant core and surface rotation rates measured in Deheuvels et al. (2014). They introduced an additive angular momentum diffusion coefficient to the transport of angular momentum equation in the radiative zone, which obeys an advection-diffusion equation:

$$\rho \frac{d}{dt} (r^2 \Omega(r)) = \frac{1}{5r^2} \frac{\partial}{\partial r} (\rho r^4 \Omega(r) U(r)) + \frac{1}{r^2} \frac{\partial}{\partial r} \left(\rho (D_{\text{shear}} + v_{\text{add}}) r^4 \frac{\partial \Omega(r)}{\partial r} \right), \quad (1.1)$$

(Zahn, 1992; Maeder & Zahn, 1998; Eggenberger et al., 2008) where r and ρ are the characteristic radius and density on an isobar. $\Omega(r)$ is the mean rotational rate and $U(r)$ is the velocity of meridional currents in the radial direction. D_{shear} is the diffusion coefficient for the angular momentum shear instability (See Equation 10 in Eggenberger et al. (2010)) and v_{add} is the additional viscosity corresponding to the excess angular momentum transport. Their results suggest that the additional angular momentum transport decreases as stars ascend the subgiant branch and increases with mass. The suggested scale of excess angular momentum transport they propose is on the order of

¹³Indeed when core rotation rates of red giants are plotted against $\log g$, a proxy for evolution, they do appear to decrease with evolution. When plotted against the more appropriate scale of mixed mode coupling (See Equation 10 in Gehan et al. (2018) and compare Figures 12 and 13 in this work), they are constant with evolution.

$10^3 - 10^4 \text{ cm}^2 \text{s}^{-1}$. Which is similar to D_{shear} close to the convective envelope but rapidly decreases to the order of $10^1 \text{ cm}^2 \text{s}^{-1}$ in the stellar core. Comparing Figures 1.7 and 1.8 we see that the introduction of the additional viscosity to the model term results agreement with the core to surface rotation fraction in the [Deheuvels et al. \(2014\)](#) sample.

[Moyano et al. \(2022\)](#) performed a similar analysis but with the core rotation rates of red giant branch and red clump stars measured in ([Mosser et al., 2012](#)) and [Gehan et al. \(2018\)](#). They found that the same order of magnitude additional viscosity term was required to explain the approximately constant core rotation rates of red giant and red clump stars. Qualitatively they found that the additional angular momentum transport becomes stronger when the star evolves up the red giant branch through shell hydrogen burning. Angular momentum must be redistributed between two to three orders of magnitude more efficiently for red clump stars than for red giants closer to the main-sequence turn-off consistent with [den Hartogh et al. \(2019\)](#). Figures 1.9 and 1.8 highlight that models of red-giant evolution with the additional viscosity introduced in this work now agree with the observed core rotation rates observed in [Gehan et al. \(2018\)](#).

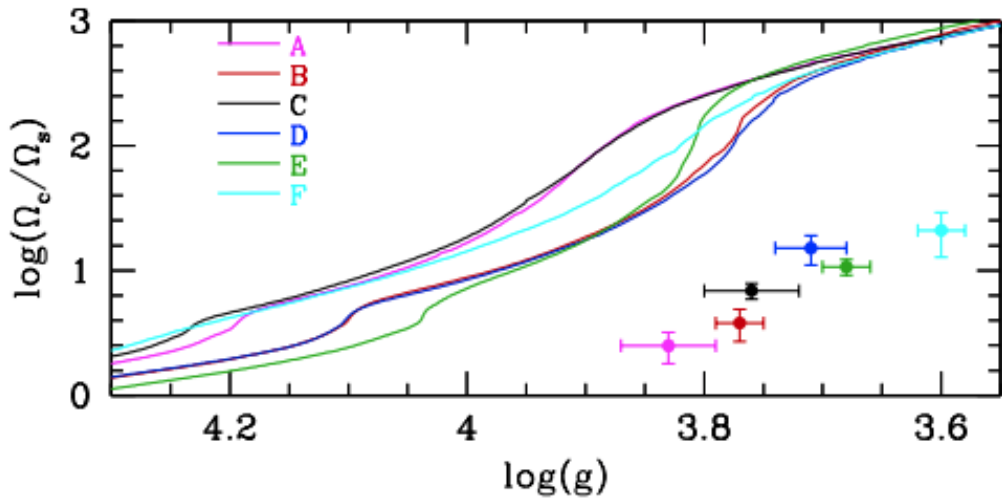


FIGURE 1.7: log of core to surface rotation rate against $\log g$. **Dots:** Observed core to surface rotation rates of the six subgiants measured in the [Deheuvels et al. \(2014\)](#) sample (A,B,C,D,E,F). **Lines:** rotating models of the stars in that sample without additional angular momentum transport ([Eggenberger et al., 2019](#)). The observed core-to-surface rotation rates are much smaller than models predict. This implies additional angular momentum transport than is currently accounted for models. Sourced from Figure 2 in ([Eggenberger et al., 2019](#)).

Several modes of excess angular momentum transport have been suggested to explain the disparity between models and observations. [Barker et al. \(2019, 2020\)](#) studied the role

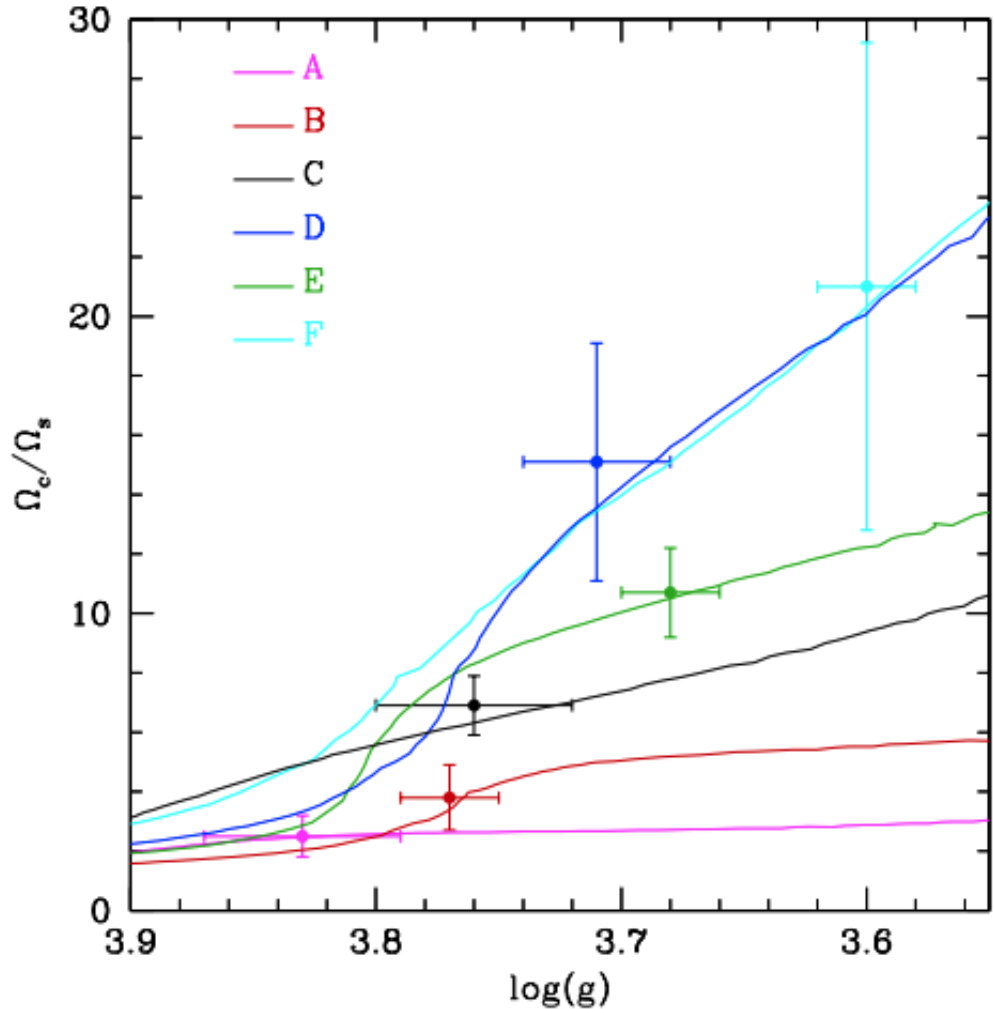


FIGURE 1.8: Same as Figure 1.7 but with additional angular momentum transport introduced for the models to reflect the observations. Sourced from Figure 3 in ([Eggenberger et al., 2019](#)).

of the Goldreich-Schuber-Fricke (GSF) instability (([Goldreich & Schubert, 1967](#); [Fricke, 1967](#)) and its role in angular momentum transport for post-main-sequence stars. They suggest that the GSF instability can introduce additional viscosity up to $10^4 \text{ cm}^2 \text{s}^{-1}$ for low-mass stars but is two orders of magnitude too small to reflect the rotation of higher mass stars not discussed in this work.

Magnetorotational instabilities constitute another candidate to explain the internal rotation of evolved stars. Two potential candidates are azimuthal magnetic rotational instabilities (AMRI) ([Ruediger et al., 2014](#); [Rüdiger et al., 2015](#)) and the Tayler-Spruit instability ([Spruit, 2002](#)) (See Section ??). [Rüdiger et al. \(2015\)](#) suggest AMRIs can increase molecular viscosity to the magnitude required to explain observations. On the

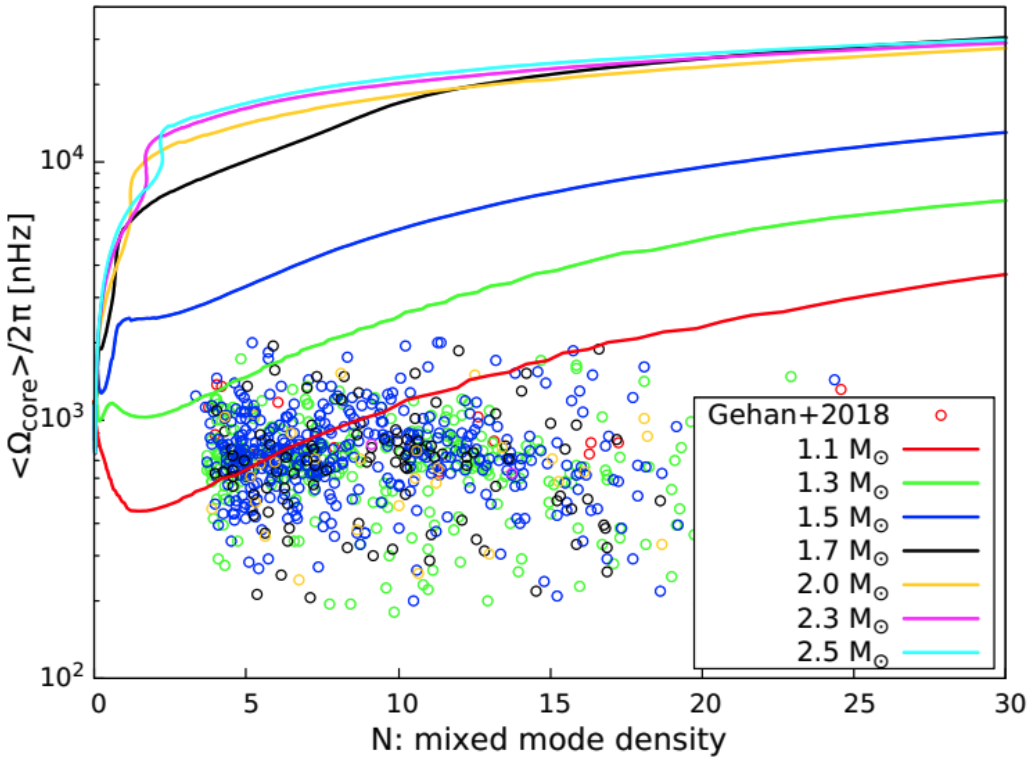


FIGURE 1.9: Average core rotation rates of red giants against mixed mode density (a proxy for evolution) **Dots:** Observed core rotation rates from Gehan et al. (2018) **Lines:** rotating models of the stars in that sample without additional angular momentum transport (Moyano et al., 2022). The observed core rates are much smaller than models predict. Implying excess angular momentum transport is required for the models to reflect the observations. Sourced from Figure 6 in (Moyano et al., 2022).

other hand, there is no evidence to suggest that this instability reflects the trends with mass and evolution. The Tayler instability does introduce excess angular momentum transport in the post-main-sequence (Fuller et al., 2019), however, it cannot simultaneously reflect the observations of both subgiants and red giants (Eggenberger et al., 2019; den Hartogh et al., 2019).

Spada et al. (2016) propose the efficiency of angular momentum transport may be related to the core to surface rotation rate to some power - $(\Omega_c/\Omega_s)^{\alpha}$ - which can be related to magnetorotational instabilities. This work suggests that $\alpha = 3$ reflects the core rotation rates of red giants claimed in (Mosser et al., 2012). Moyano et al. (2022) revisited this prescription and found that $\alpha = 3$ more accurately reflects the approximately constant rotation core rotation rates of red giants observed by Gehan et al. (2018). Spada et al. (2016) was limited to a single model with mass = $1.25 M_{\odot}$. No parameterisation with mass was therefore performed.

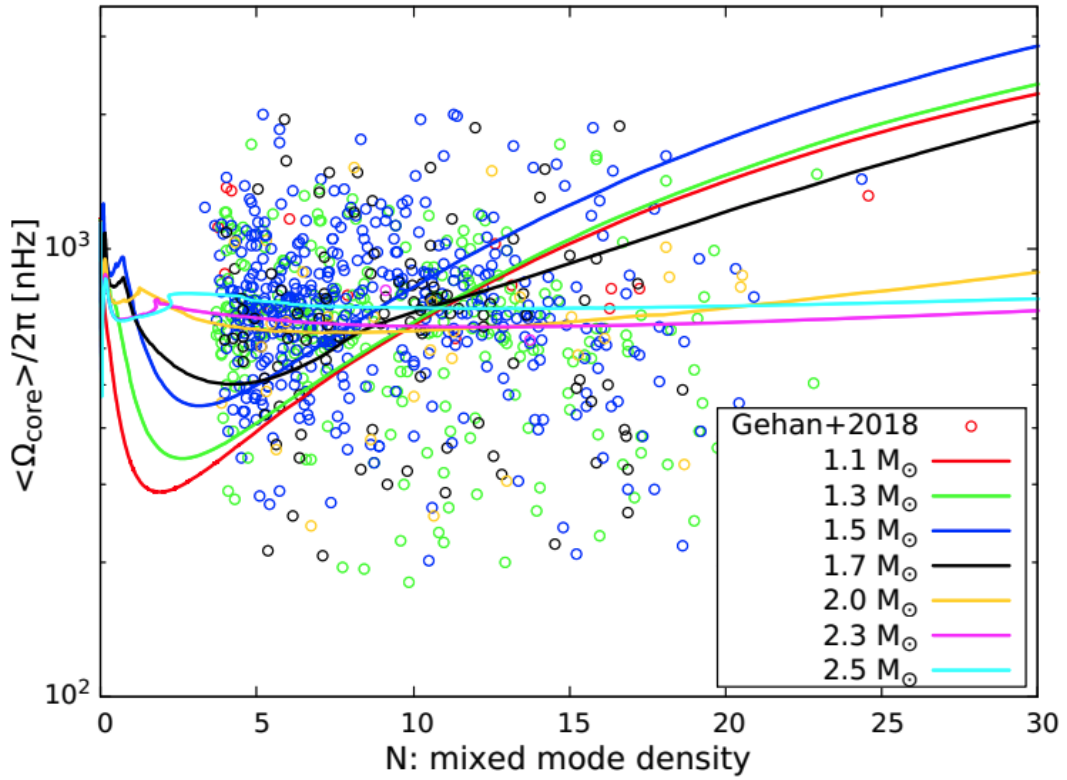


FIGURE 1.10: Same as Figure 1.9 but with additional angular momentum transport introduced for the models to reflect the observations. Sourced from Figure 7 in ([Moyano et al., 2022](#)).

Other physical mechanisms have been suggested to have a role in excess angular momentum transport, such as angular momentum transport by internal gravity waves ([Pinçon et al., 2017](#)) or mixed-modes ([Belkacem et al., 2015](#)). However, the scale of their introduced additional viscosity is yet to be investigated. Disentangling each of these proposed mechanisms' relative importance to the additional angular momentum transport required to explain the observations requires much more data.

We speculate that the simultaneous measurement of subgiants' core and surface rotation rates may be the best probes for constraining the excess angular momentum transport. A few pathways exist to further probe the mechanism underlying excess angular momentum transport through asteroseismology alone. Either: a) more stars need to have their core and surface rotation rates measured through asteroseismology (which we will denote ensemble fitting), or b) stronger constraints must be placed on the rotation profile between the core and the surface (single star constraints).

On the former, if more stars have their core and surface rotation rates observed, then

more measurements of the excess angular momentum transport required for state-of-the-art models to match the observations are made. The excess angular momentum transport required to match observations appears mass and evolutionary-dependent. Stronger constraints to the dependency of the excess angular momentum transport on these quantities provide information about the underlying mechanism. The Kepler asteroseismic data currently available suggests that the efficiency of the excess angular momentum transport increases with the star's mass (Eggenberger et al., 2019). However, the efficiency of angular momentum transport decreases with evolution during the subgiant phase. Consequently, a transport process with efficiency dependent on the angular momentum gradient between the core and the surface cannot be at play in subgiants. Identifying with more precision the dependency of excess angular momentum transport on stellar quantities would provide evidence for or discredit proposed mechanisms.

On the latter, the internal shape of the rotation profile of subgiants reflects the underlying mechanism that created it. Therefore, evidence for or against particular shape of rotation profiles is illuminating to proposed mechanisms. A strong gradient in the rotation profile in the core of a subgiant, for example, is incompatible with angular momentum transport through deep fossil magnetic fields (Gough & Thompson, 1990) as they would likely smooth out sharp features. This is because differential rotation is expected to be damped along poloidal field lines (Garaud, 2002; Strugarek et al., 2011). Internal gravity waves, on the other hand, are expected to be efficient during the advanced phases of stellar evolution (Charbonnel & Talon, 2008). Internal gravity waves can give birth to localised weak gradients in the rotation profile as a result of extraction and deposit of angular momentum (Charbonnel & Talon, 2005). A sharp rotational gradient could also potentially trigger magneto-rotational instabilities that would transport angular momentum (Balbus & Hawley, 1994; Arlt et al., 2003; Menou & Mer, 2006; Fuller et al., 2015, 2019; Moyano et al., 2022). Evidence of a strong angular momentum gradient towards the core of a sub-giants quickly constrains the number of possible angular momentum transport mechanisms to solve the angular momentum transport problem.

Two obvious problems impede the single-star pathway. These are the need for observations of high SNR higher degree modes and the results of methods used to measure

rotation profiles being unstable to high-resolution inversions. Constraints on the rotation profile in intermediate points between the core and surface require the observations of oscillation modes of $l \approx 10$ (Ahlborn et al., 2020). For reliable measurements of such oscillations, much longer observation periods, longer than *CoRoT* and *Kepler*, of sub-giants are required.

Both of these pathways require much more asteroseismic data than is currently available. For ensemble fitting to be viable many subgiants would need to be observed over long baselines with short cadence observations. If the Kepler mission is exemplary, then the baseline required for high-SNR asteroseismic observations is on the order of 4 years per star.

At the time of writing, 30 subgiants show evidence of rotational splittings (Li et al., 2020b,a), though the rotational splitting data is yet to be released and analysed. The results will be undoubtedly informative, though we will not speculate exactly how much they will solve the subgiant excess angular momentum transport problem. Hatt et al. (2023) suggests that there is ~ 4000 stars in the TESS - short cadence catalogue with observable solar-like oscillation features. The measured frequency of peak oscillation power ν_{\max} of stars in these sample suggests that some of these stars are subgiants. While no rotational splittings of these stars have been reported some of these stars may lay in the continuous viewing zone. This means their observation periods are approaching 4 years at time of writing and these stars may soon offer a separate sample of subgiants with observations of asteroseismic rotational splittings. While we may speculate about future asteroseismic focussed missions, it will be some time before any new asteroseismic rotation signals in subgiants are made.

Independent constraints can also be placed on the evolution of the surface rotation of subgiants. Santos et al. (2021) measured the surface rotation of 4500 subgiants using photometric oscillations from stellar spots. The measured rotational periods against their effective temperature are shown in Figure 1.11. Within this Figure, there are a few notable features. While subgiants are definitionally older than their main-sequence counterparts, there is a sample of fast-rotating stars coincident with the fast rotators on the main sequence. This could be explained by most of the stars in this sample being a higher mass than the Kraft break. They have passed through the main sequence with fast rotating surfaces, entering the subgiant phase; their effective temperatures decrease

and are shifted to the right in this diagram relative to their main-sequence counterparts. The high density of fast-rotating stars could also result from an observational bias. Long rotational periods require longer baselines to recover and thus have a decreased observed fraction. Among the sample is a group of slow-rotating (Period > 60 days) targets with Teff between 5000 and 6000 K. These are consistent with more evolved subgiants as the slowest of these targets are located close to the red giant branch. This work also suggests that the decreased observation of rotation periods >60 days, the strong upper edge of the [McQuillan et al. \(2014\)](#) rotational period distribution, is the result of a lack of observations of main-sequence stars rather than an inherent lack of long period probing power by *Kepler*. Whether the upper edge results from angular momentum transport or decreased photometric variability is unknown. The final feature that is not commented on in their work is an apparent dearth of observations coincident with the intermediate period gap. Whether this is real or a result of noise is an interesting avenue of research in further understanding the underlying mechanism of the intermediate period gap for main sequence stars.

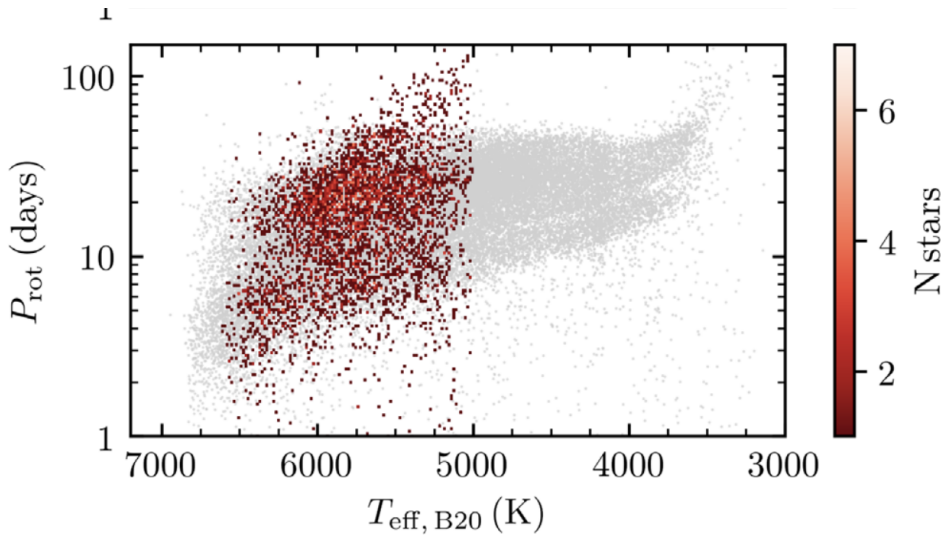


FIGURE 1.11: Surface rotation period against effective temperature of subgiants in the [Santos et al. \(2021\)](#) sample overlayed over the *Kepler* [McQuillan et al. \(2014\)](#) sample. Sourced from the bottom panel of Figure 5 in ([Santos et al., 2021](#)).

[Ceillier et al. \(2017\)](#) measured the surface rotation periods of 361 red giants from stellar spot photometric variability. The measured rotational periods against their mass are shown in Figure 1.12. Expectedly, comparative to the subgiant analysis of [Santos et al. \(2021\)](#) the surface rotation period of red giant stars is greater than their subgiant counterparts. They suggest that the surfaces of these stars rotate faster than models

suggest ([Tayar et al., 2015](#)). They conclude that the large percentage of rapid rotators must result from interactions of red giants with other bodies. This work, however, is older than the revised excess angular momentum transport research discussed earlier in this work. Their results need to be reexamined within the context of excess angular momentum transport.

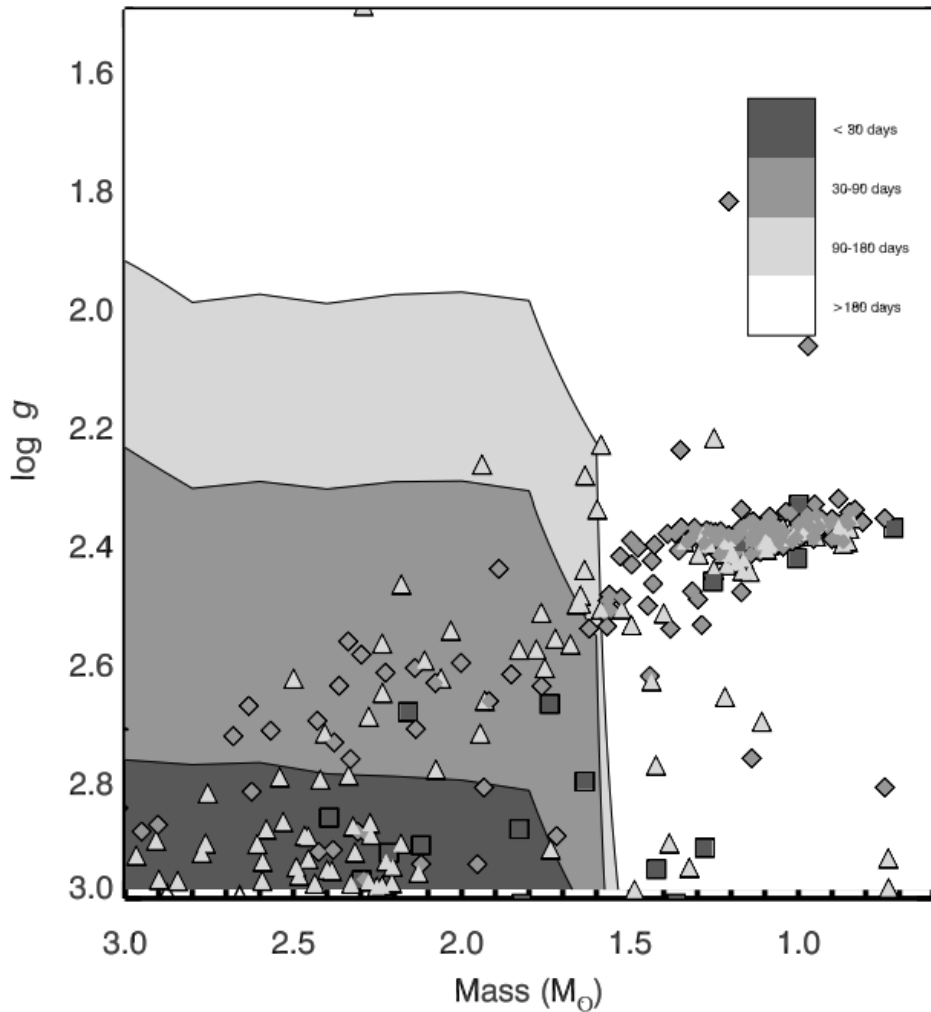


FIGURE 1.12: Surface rotation period against mass of red giant stars from [Ceillier et al. \(2017\)](#). Sourced from the top panel of Figure 7 in ([Ceillier et al., 2017](#)).

Finally, we discuss the rotating remnants of low-mass post-main-sequence evolution: white dwarfs. White dwarfs do not evolve rotationally, though their observed rotation rates constrain angular momentum during the red clump phase. [Hermes et al. \(2017\)](#) suggest that the rotation periods of white dwarfs decrease with the progenitor's mass. As previously discussed, the surface rotation rates of white dwarfs are consistent with angular momentum conservation following the red clump ([den Hartogh et al., 2019](#);

[Cantiello et al., 2014](#)). This is because the time scale of angular momentum transport is longer than the timescale of evolution from red clump star to a white dwarf. [den Hartogh et al. \(2019\)](#) suggest that mass-dependent angular momentum transport must decrease with evolution along the red clump such that the angular momentum of terminal red clump rotation cores agree with the angular momentum of white dwarf stars.

1.3 Effects of rotation

Within the previous Section, we discussed the evolution of rotation from birth to remnants of evolution. While we now have an understanding of this evolution, we still need to clarify the effects of rotation on stellar evolution.

1.3.1 Hydrostatic effects

The effects of rotation on stellar evolution are varied and complex. In general, the hydrostatic effects of rotation have only minimal effects on the internal evolution of stars ([Kippenhahn et al., 1970; Maeder & Meynet, 2000](#)). Especially the low-mass, slowly rotating stars we consider in this work. In this Section, we review how some of these effects are treated in current models of stellar evolution, the resulting changes to stellar evolution brought about by these effects and their observable consequences. We will begin by discussing the effects of stellar rotation on hydrostatic equilibrium.

As a star rotates, its equilibrium configuration deviates from the non-rotating hydrostatic equilibrium due to centrifugal forces. Rotation-induced centrifugal forces induce deviations from spherical symmetry. Only if the rotation energy of a star approaches a significant fraction of the gravitational potential energy will observable triaxial deformation occurs. Low-mass stars usually rotate slowly, so these effects are rarely seen.

The four equations of stellar structure need to account for this change to the equilibrium configuration. [Kippenhahn & Thomas \(1970\)](#) devised the method to account for this where a conservative potential exists. In this method, they replace the notion of spherical stratification of non-rotating stars with a rotationally deformed shellular stratification where the structural variables - e.g. pressure (P), density (ρ), temperature (T), chemical abundances - are constant on an equipotential. The equipotential in this prescription is

defined as $\Psi = \Phi + \frac{1}{2}\Omega^2 r^2 \sin^2 \theta$, the non-rotating gravitational potential modulated by the centrifugal force, where Φ is the gravitational potential, θ the latitude relative to the rotational axis and Ω the angular rotation rate. This method applies only when a conservative potential exists, i.e. when the angular velocity distribution is cylindrically symmetric (Tassoul, 1978). The internal rotation generally evolves towards rotation laws that are non-conservative. For example, Zahn (1992) suggests that turbulence is anisotropic, with a stronger transport horizontally than vertically. This results in a constant rotation rate on isobars and does not fall into the conservative case. ? revise Kippenhahn (1974)'s method and prescribe a consistent description of shellular rotation on isobars which is valid for slow rotation. On these isobars, the non-rotating stellar variables and angular momentum are constant. This allows models of rotating stellar evolution to be kept one-dimensional.

The equations of stellar structure are mainly affected by rotation through a few key concepts. Centrifugal forces reduce effective gravity for all points in the star that are not on the axis of rotation. The centrifugal forces vary with radial distance and latitude, resulting in equipotentials closer together along the rotational axis than the equatorial axis. Radiative flux varies with local effective gravity (von Zeipel, 1924). This results in gravitational darkening (von Zeipel, 1924; Kippenhahn, 1977) - stars are higher temperature and have larger temperature and radiation flux along the rotational axis compared to the equatorial axis. Gravity darkening of slowly rotating stars (rotation rates much slower than the break-up velocity like those considered in this work) is very small - <<0.1% variation in luminosity and temperature across their surfaces. Stars close to critical rotation rate should be treated with care (Kippenhahn, 1977; Maeder, 1999; Heger et al., 2000).

1.3.2 Increased mixing in stars

Rotation can extend the mixing regions in stars - allowing mixing between the radiative core and convective envelope - and increase the mixing efficiency through meridional circulation and rotational instabilities.

For convenience, throughout the following Section, we make use of the following gradients:

$$\nabla_{\text{ad}} := \left(\frac{\partial \ln T}{\partial \ln P} \right)_{\text{ad}}, \quad \nabla_\mu := \frac{d \ln \mu}{d \ln P}, \quad \nabla := \frac{d \ln T}{d \ln P} \quad (1.2)$$

$$\delta := - \left(\frac{\partial \ln \rho}{\partial \ln T} \right)_{\mu, P}, \quad \varphi := \left(\frac{\partial \ln \rho}{\partial \ln \mu} \right)_{P, T}, \quad (1.3)$$

where μ is the mean molecular weight at a given position in a star. The subscript "ad" refers to the gradient if we adiabatically transported a fluid element along a path. ∇ is simply the temperature gradient relative to the pressure gradient, ∇_{ad} is our temperature gradient relative to the pressure gradient along an adiabat, that is, the temperature gradient that arises from adiabatically transporting fluid elements along P , ∇_μ is the composition gradient with relative to the changing pressure, δ is the density gradient relative to the temperature along paths of constant μ and P and φ is the density gradient relative to the mean molecular weight along paths of constant P and T .

In non-rotating stars, mixing can be simplified by whether a region in a star is convective, semi-convective, radiative or undergoing thermohaline mixing (These concepts will not be discussed at length in this work. See [Maeder & Meynet, 2000](#); [Tassoul, 2000](#), for good overviews of these concepts.) Convective regions are well mixed and have no chemical gradients, as convection acts on local dynamical time scales, while radiative regions are not well mixed and are generally chemically stratified. Semi-convective regions are thermally unstable regions stabilised against convection by a gradient in composition. Thermohaline mixing arises when an unstable gradient in composition (mean molecular weight) is only partially stabilised by thermal stability. Semi-convection and thermohaline mixing act on longer time scales than convection; their effective diffusion coefficient is smaller. The conditions required for semi-convection and thermohaline mixing are well discussed in the works referenced above. Here we will focus on convective and radiative regions for simplicity. Whether a region is convective or radiative is defined by whether the Brunt-Väisälä frequency, the characteristic oscillation frequency of a displaced particle of fluid in a stratified density medium is positive or negative.

$$N^2 = \frac{g\delta}{H_P} \left(\nabla_{\text{ad}} - \nabla + \frac{\varphi}{\delta} \nabla_\mu \right), \quad (1.4)$$

where H_P is the local pressure scale height ($H_P = \frac{P}{\rho g}$ in hydrostatic equilibrium, where P is local pressure, ρ is local density and g local effective gravity). Rotation can overcome the pressure, density and mean molecular weight gradients to push mixing into previously stable regions through rotational instabilities.

When we discuss the Brunt-Väisälä frequency, it is worth thinking of the characteristic

oscillations of mass parcels. When the Brunt-Väisälä frequency is negative, the oscillations grow exponentially, leading to enhanced mixing. The mixing process is treated as essentially instantaneous in models. When it is positive, the oscillations are bounded, and mixing does not occur. On the other hand, when the Brunt-Väisälä frequency is negative but very close to zero, the oscillations grow slower than in the case of convection. While some instabilities act on dynamical time scales, we do not treat diffusion due to instabilities as if they were convective. In that way, we separate the effect of instabilities by their contribution to the total effective diffusion at every point in a star.

Here we will briefly discuss a non-exhaustive list of rotational instabilities and how they impact the mixing of stars. Most of these instabilities are not expected to arise during the low-mass ($<8M_{sol}$) main-sequence evolution due to the small angular momentum gradients of main-sequence stars, as discussed in the previous Section. However, they are influential during evolutionary periods where strong rotational gradients arise: during the post-main-sequence or core envelope decoupling as suggested in some models of young-main sequence evolution (Heger et al., 2000).

We separate the instabilities by the timescale. They act upon dynamic and secular instabilities. We expect secular instabilities to act on during the main sequence when rotational gradients are small and evolutionary times scales are long. On the other hand, strong rotational gradients arise during the post-main-sequence. Dynamical instabilities also act on shorter timescales than evolutionary timescales in the post-main-sequence. As a result, dynamical instabilities are mainly expected to play a role during the post-main-sequence.

1.3.2.1 Dynamical shear instability

The dynamical shear instability arises when the energy that can be gained from a shear flow (a rotational gradient) is comparable to the work that must be done to displace a mass element adiabatically. This means the instability is inhibited by density gradients but is very effective along isobars (Endal & Sofia, 1978; Pinsonneault et al., 1989; Heger, 1998), supporting the shellular isobaric representation of rotation in stellar models.

The condition for stability is dependent on the local rotational gradient modulating the Brunt-Väisälä frequency:

$$Ri = \frac{g\delta}{H_P} \left(\nabla_{ad} - \nabla + \frac{\varphi}{\delta} \nabla_\mu \right) \left(g \frac{d \ln r}{d\Omega} \right)^2 > Ri_C, \quad (1.5)$$

where ω is the angular rotation rate and Ri_C is the critical Richardson number = 1/4 (Zahn, 1974). The region is considered stable if $Ri > Ri_C$, and the diffusion coefficient is 0. When unstable, the diffusion coefficient is proportional to the extent to which the rotational gradient overcomes the chemical and temperature gradients, Ri/Ri_C , the spatial extent of the unstable region, and the local dynamical timescale.

1.3.2.2 Solberg-Høiland instability

The Solberg-Høiland instability occurs when introducing the centrifugal force to the net force on an adiabatically displaced mass element overcomes the thermal and chemical gradient stabilities. The condition for stability is given by:

$$R_{SH} = \frac{g\delta}{H_P} \left[\nabla_{ad} - \nabla + \frac{\varphi}{\delta} \nabla_\mu \right] + \frac{1}{r^3} \frac{d}{dr} (r^2 \Omega)^2 \geq 0, \quad (1.6)$$

The second term in the equation accounts for the introduction of rotation, where the specific angular momentum (j) is $r^2\Omega$ (Tassoul, 1978; Kippenhahn & Weigert, 1990; Heger et al., 2000). Under no rotation (or no angular momentum gradient), we recover the Brunt-Väisälä frequency.

For the Solberg-Høiland instability to occur, the second term in the equation must be negative and, therefore, only occurs in regions of decreasing angular momentum (a negative rotation gradient with respect to radius). The diffusion coefficient associated with this instability increases with R_{SH} - the more the angular momentum gradient overcomes the thermal stability, the greater the mixing effect -the spatial extent of the unstable region, the local dynamical timescale.

1.3.2.3 Secular shear instability

When thermal dissipation is significant, the restoring force of buoyancy is reduced, and the strict criteria for the dynamical shear instability to act can be relaxed. Due to

this process requiring thermal dissipation, it operates on the relatively slower (secular) thermal-time scale, hence its name.

[Endal & Sofia \(1978\)](#) suggest two stability conditions against secular shear instability. The first is a modulation to the thermal stability component of the Brunt-Väisälä frequency by a product of the Reynolds number - a dimensionless fluid flow number - and Prandtl number (P_E):

$$R_{is,1} = P_E \frac{g\delta}{H_P} (\nabla_{ad} - \nabla) \left(g \frac{d \ln r}{d\Omega} \right)^2 > Ri_C, \quad (1.7)$$

where $P_E = \frac{Pr R_{e,c}}{8}$. $R_{e,c}$ is the critical Reynolds number of the flow of material, and Pr is the Prandtl number, the ratio of the thermal diffusion timescale to the angular momentum diffusion timescale (See [Tassoul, 1978](#); [Heger, 1998](#), and references therein for a more thorough explanation of these quantities and their implementation in models of stellar rotation).

The second condition is the mean molecular weight component of the dynamical shear instability, which is not affected by the relaxation of thermal adjustment

$$R_{is,2} = \nabla_\mu \frac{g\varphi}{H_P} \left(g \frac{d \ln r}{d\Omega} \right)^2 > Ri_C. \quad (1.8)$$

The need for the inclusion of this term is debated, however.

[Endal & Sofia \(1978\)](#) suggest that the diffusion coefficient scales with the characteristic velocity of the secular shear instability, the characteristic scale height - the combination of which provides the characteristic timescale - and either $R_{is,1}$ and $R_{is,2}$ whichever violates the criteria more.

Many works have shown that the molecular gradient inhibits mixing by up two orders of magnitude than observations suggest. Those who include the term include a factor on ∇_μ of order < 0.05 to account for this ([Charbonnel et al., 1994](#); [Heger et al., 2000](#)).

[Maeder & Meynet \(1997\)](#) argues that the regions where molecular gradients are strong enough to inhibit mixing from the secular shear instability, near the core, are generally semi-convective and experience some mixing/turbulence already. They suggest that in a semi-convection region (or in any zone with other sources of turbulence), some fraction of the local energy excess in the shear is degraded by turbulence to change the local

entropy gradient. They hypothesise that this turbulence will affect the shear energy and molecular gradient and calculate a diffusion coefficient under this assumption. They find that the diffusion coefficient is consistent with the semi-convective diffusion coefficient when turbulence overcomes the shear and towards $K/R_{is,1}$ when semi-convection is negligible (Consistent with the results of [Zahn, 1992](#)). [Talon & Zahn \(1997\)](#), on the other hand, account for the mixing effect of horizontal diffusion from semi-convection on the restoring force produced by the molecular gradient, which reduces its stabilising effect. Both works result in the diffusion of elements consistent with observations without adding new factors.

1.3.2.4 Meridional circulation

Meridional circulation ([Eddington, 1925](#)) arises from gravity darkening. Excess flux along the rotational axis heats material more than along the equator. This drives the large-scale circulation of material from the pole to the equator. This results in angular momentum transport and chemical transport. Early theoretical considerations of meridional circulation were not physically consistent. They predict inverse circulation (from the equator to the axis of rotation) close to the surface, and they did not conserve angular momentum ([Sweet, 1950](#); [Mestel, 1953](#); [Mestel & Spitzer, 1956](#); [Kippenhahn & Weigert, 1990](#)).

Meridional circulation can be treated differently for the transport of elements and the transport of angular momentum. [Endal & Sofia \(1978\)](#) derived a In this prescription, the diffusion coefficient scales with the Eddington-Sweet velocity and the extent of the region where the process is in effect (See [Kippenhahn, 1974](#); [Endal & Sofia, 1978](#); [Heger et al., 2000](#)).

On the other hand, [Zahn \(1992\)](#) determined that energy conservation, gravity and angular momentum much be calculated simultaneously for a self-consistent and physically possible solution to be found. [Chaboyer & Zahn \(1992\)](#) showed that if the horizontal component of turbulence is large, the effects of meridional circulation on the transport of elements is equivalent to a diffusion process with diffusion coefficient D_{mr} .

$$D_{mr} = \frac{|rU(r)|^2}{30D_h} \quad (1.9)$$

D_h is the coefficient of horizontal turbulence, $U(r)$ is the vertical component of the meridional circulation velocity, and r is the radius at which the components are calculated. While diffusion from horizontal turbulence is required for meridional circulation to be treated as a diffusive process, it is also inhibited.

Measurements of the Lithium-7 abundance in the sun support this prescription. The difference between the derived diffusion coefficients from Kippenhahn (1974); Endal & Sofia (1978); Heger et al. (2000) and Chaboyer & Zahn (1992) prescriptions is approximately a factor of 30 scaling. Pinsonneault et al. (1989) found that a scaling of 0.046 ($\sim 1/30$) of the Kippenhahn (1974) diffusion coefficient is required to reproduce the observed Lithium-7 abundances. Indeed the two prescriptions are appropriate with sufficient scaling.

Prescriptions for horizontal diffusivity (D_h) are lacking in physical motivation. Zahn (1992) suggests $|rU(r)|$ is an adequate prescription. Maeder (2003) derived an expression with respect to energy considerations, while Mathis & Zahn (2004) adapted a prescription from laboratory experiments. Mathis et al. (2018) suggest that the anisotropy of turbulent transport scales as $N^4\tau^2/(2\omega^2)$, where N and ω are the Brunt-Väisälä and rotation frequencies and τ the time scale characterising the source of the turbulence. Their results all generally agree though this does not suggest that they are the correct formalisation of horizontal diffusion.

Angular momentum transport by meridional circulation can be treated as an advective or diffusive process. Consider the path of a fluid element along a meridional eddy. Meridional circulation describes a rise of material along the rotational axis, descending at the equator. This results in the transport of angular momentum *against* the angular momentum gradient. On the other hand, implementing angular momentum transport as a wholly diffusive process is numerically simpler (Endal & Sofia, 1978; Pinsonneault et al., 1989; Heger et al., 2000). The two implementations may deviate in regions where meridional circulation dominates. The two implementations obtain similar results along the main-sequence (Talon & Zahn, 1997; Heger et al., 2000) where the evolutionary timescale is long enough for meridional circulation to be impactful.

[Zahn \(1992\)](#) derived the radial component of the velocity of meridional circulation ($U(r)$) under the effects of thermal and molecular weight gradients.

$$U(r) = \frac{1}{H_P C_P T [\nabla_{\text{ad}} - \nabla + (\varphi/\delta) \nabla_\mu]} \left(\frac{L}{M} (E_\Omega + E_\mu) \right), \quad (1.10)$$

where C_P is the specific heat and E_Ω and E_μ are terms dependent on up to the third order derivatives of the rotational distribution and molecular mass distribution (See [Maeder & Zahn, 1998](#)). This prescription for meridional circulation resolves the inverse circulation of earlier prescriptions and conserves angular momentum.

1.3.2.5 Goldreich-Shubert-Fricke instability

The Goldreich-Shubert-Fricke (GSF) instability arises when a fluid is unstable to axisymmetric displacements ([Goldreich & Schubert, 1967](#); [Fricke, 1967](#)). Stars tend to be inviscid, $P_R \ll 1$. Under this assumption [Kippenhahn et al. \(1970\)](#) derives two conditions for stability. The first is the secular analogue of the Solberg-Høiland condition for stability under the assumption that the stability from the temperature gradient is removed by thermal conduction

$$\frac{\partial j}{\partial r} \geq 0. \quad (1.11)$$

The second is an analogue to the Taylor-Proudman theorem for slowly rotating incompressible fluid [Kippenhahn \(1974\)](#); [Tassoul \(1978\)](#); [Heger et al. \(2000\)](#).

$$\frac{\partial \Omega}{\partial z} = 0, \quad (1.12)$$

where z is the distance along the rotational axis. Fluids are well mixed along equipotentials. As discussed concerning the Von-Zeipal effect, equipotentials are closer along the rotational axis. Along an equipotential, if the rotation rate gradient is non-zero, then fluid will be mixed along said equipotential until the rotation profile is conservative. Stability favours uniform rotation on equipotentials, which is incompatible with shellular rotation except under solid-body rotation. The GSF instability, therefore, tends to enforce uniform rotation on thermal timescales ([Endal & Sofia, 1978](#)).

The GSF instability demands mixing from meridional circulation and thus, like meridional circulation, acts on the circularisation timescale.

1.3.3 Magneto-rotational instabilities

The role of magneto-rotational instabilities in the rotation of stars is debated. In this Section, we will discuss the theory behind a few of these instabilities and their effects in reference to the post-main-sequence rotational evolution.

Models of post-main-sequence rotational evolution with magnetorotational angular momentum transport suggest that the rotational profile of stars that have undergone significant angular momentum transport track include a strong rotational gradient following the H-burning shell (Fuller et al., 2019; Moyano et al., 2022).

1.3.3.1 Tayler instability and the Spruit Dynamo

The Tayler instability arises from the interaction between rotation and magnetic fields in a conducting fluid. If the magnetic field is aligned with the rotation axis, the Coriolis force tends to twist the field lines into a helical shape. This can lead to a buildup of tension in the field lines, which can trigger a series of instabilities that amplify the magnetic field. The end result is a complex pattern of magnetic fields that can drive large-scale flows in the fluid.

The Spruit dynamo, on the other hand, arises from the interaction between rotation and shear flows in a rotating fluid (Spruit, 2002). A radial gradient in the rotation rate can generate a shearing motion that can stretch and amplify the magnetic field lines. This process can lead to the buildup of magnetic energy and the generation of large-scale magnetic fields.

Combining these two mechanisms can lead to forming a self-sustaining magnetic dynamo in rotating stars (Spruit, 1999). The Tayler instability can amplify the magnetic field on small scales, while the Spruit dynamo can amplify the magnetic field on large scales. The resulting magnetic fields can drive large-scale flows in the fluid, which in turn can modify the rotation rate and generate new instabilities (Fuller et al., 2015, 2019)

The instability could be effective even if the initial field strength is small (Spruit & Phinney, 1998). Unfortunately, little is known about the initial field's strength and the efficiency of instabilities in amplifying the magnetic field. Fuller et al. (2019) suggests

that the Tayler-Spruit instability could play a role in the post-main-sequence angular momentum transport problem discussed in Section 1.2.

1.3.3.2 Azimuthal Magnetorotational instability

The azimuthal magnetorotational instability (AMRI) is a type of instability that can arise in rotating, magnetised plasmas (Hollerbach et al., 2010). It is a variation of the more well-known magnetorotational instability (MRI), which occurs when a weak magnetic field is present in a rotating fluid or plasma.

The AMRI occurs when the magnetic field is not aligned with the rotation axis but is instead perpendicular to it. This can happen in astrophysical systems where the magnetic field is generated by a dynamo mechanism or is inherited from the system's initial conditions. In such cases, the AMRI can become the dominant instability, driving large-scale fluid motions and enhancing the transport of angular momentum (Mishra et al., 2021; Moyano et al., 2022).

The basic idea behind the AMRI is that the magnetic field can act as a free energy source that fluid motions can tap. If the magnetic field is perpendicular to the rotation axis, it can introduce a new length scale into the system, leading to a wider range of unstable modes. This can result in the growth of perturbations not present in the MRI, leading to more complex dynamics.

The AMRI's strength depends on a star's internal degree of differential rotation. Moyano et al. (2022) has discussed the role of the AMRI in relation to the post-main-sequence angular momentum transport problem. They suggest that a consistent prescription of the AMRI dependent on the degree of internal differential rotation could explain the observed core and surface rotation rates of subgiants and red giants that have not reached the red giant bump.

1.3.4 Other angular momentum transport mechanisms

Here we describe other angular momentum transport mechanisms that are not instabilities but may play a role in the evolution of stellar rotation.

One of these mechanisms is angular momentum transport by internal gravity waves (IGWs) (Pantillon et al., 2007; Kim & MacGregor, 2000; Talon & Charbonnel, 2005; Charbonnel & Talon, 2008) IGWs are internal propagation waves that can carry angular momentum from the core to the surface of stars.

Buoyancy forces in a stratified fluid drive internal gravity waves. In a rotating fluid, these waves can become distorted by the Coriolis force, leading to the angular momentum transfer between different fluid layers. The wave motion can induce a net angular momentum flux, leading to changes in the rotation rate (Zahn, 1975).

One key aspect of this theory is the identification of the so-called "critical layers", which are regions where the wave frequency matches the local rotation frequency. These layers can lead to a resonance between the wave and the rotation, leading to enhanced transport of angular momentum (Charbonnel & Talon, 2005).

The characteristic rotation profile that would suggest IGWs are at play is a strong rotational gradient tracking the H-burning shell (Balbus & Hawley, 1994; Menou & Mer, 2006).

Another mechanism that may play a role in post-main-sequence angular momentum transport is the transport of material by mixed modes (Belkacem et al., 2015). Comparative to the main sequence, post-main sequence stars express mixed modes when only pressure (p) waves propagate in the surface (convective) region. Mixed modes are gravity (g) modes that are usually constrained to the radiative core that have coupled with p modes.

Belkacem et al. (2015) suggests this process can extract angular momentum from the core of subgiants and red giants.

The efficiency of this angular momentum transport mechanism grows with the radial differential rotation gradient within stars and is thus strongest for red giants. Their results of this work suggest that while this mechanism may be at play, it is not strong enough to account for the observed core and surface rotation rates of subgiants.

1.3.5 Implementation of diffusive processes in models of rotating stellar evolution

1.3.5.1 Transport of Angular momentum

Angular momentum is transported by convection, mixing by instabilities and meridional circulation. The equation for the transport of angular momentum between shells, as an advective process, is

$$\rho \frac{d}{dt} (r^2 \Omega(r))_{M_r} = \frac{1}{5r^2} \frac{\partial}{\partial r} (\rho r^4 \Omega(r) U(r)) + \frac{1}{r^2} \frac{\partial}{\partial r} \left(\rho (D_{\text{tot}}) r^4 \frac{\partial \Omega(r)}{\partial r} \right), \quad (1.13)$$

where subscript M_r is the mass coordinate at a radius (r), ρ is the local density, $U(r)$ is given by Equation 1.10, $r^2 \omega$ is the angular momentum, and D_{tot} is the sum of the diffusion coefficients from the various diffusion processes discussed in the previous Section. The factor of 1/5 comes from the integration with respect to latitude (Zahn, 1992; Maeder & Zahn, 1998; Maeder & Meynet, 2000; Eggenberger et al., 2008).

The first term on the right-hand side accounts for angular momentum transport by meridional circulation. The second accounts for the transport of angular momentum by mixing processes. If meridional circulation is treated as a diffusive process then the first term is lost and the sum of the diffusion coefficients gains a meridional circulation term from Equation 1.9.

Equation 1.13 is subject to the boundary conditions at a star's core and surface. The core is subject to the boundary condition that $\frac{\partial \omega}{\partial r} = 0$ (Talon & Zahn, 1997; Denissenkov et al., 2010). The surface boundary condition can be treated in several ways. One way is to treat the boundary condition the same as the core, where no angular momentum is lost from the surface. On the other hand, the surface can be treated as an angular momentum sink. Mass loss by winds and the coupling of the mass loss to the magnetic field transport angular momentum away from the surface of a star. In the latter scenario

$$\rho \frac{d}{dt} (r^2 \Omega(r))_{\text{surf.}} = j_{\text{winds}}. \quad (1.14)$$

The rotation profile of a star is not chosen. Generally speaking, the initial condition is a flat rotation profile at the zero-age-main-sequence, which can evolve with time

due to angular momentum transport by meridional circulation, diffusive processes, and contraction or expansion. These processes' rotation profile changes are then accounted for by the angular momentum transport mechanisms - which are dependent on the rotation profile. As a result, a self-consistent solution for the evolution of the rotation profile is created.

1.3.5.2 Transport of Elements

Unlike angular momentum transport, the transport of elements can be treated as a diffusive process (Endal & Sofia, 1978; Heger et al., 2000)

Under this assumption, change in mass fraction X_i of chemical species i is

$$\left(\frac{dX_i}{dt} \right)_{M_r} = \left(\frac{\partial}{\partial M_r} \right)_t \left[(4\pi r^2 \rho)^2 D_{chem} \left(\frac{\partial X_i}{\partial M_r} \right)_t \right] + \left(\frac{dX_i}{dt} \right)_{nuc}, \quad (1.15)$$

where subscripts denote where each component is calculated, M_r is the mass coordinate at a radius (r), ρ is the local density, D_{chem} is the total mixing coefficient from turbulent diffusion processes and the effective diffusion coefficient from meridional circulation ($D_{chem} = D_{tot} + D_{MR}$).

The first term reflects the mixing of elements, and the second accounts for the change in elemental abundances from nuclear reactions.

1.3.6 Stellar Winds

Mass loss can significantly affect the evolution of stars, especially in massive stars (?). Rotation enhances the loss of mass through stellar winds of stars.

Friend & Abbott (1986); Langer (1991); Heger (1998) suggest that the mass loss rate of rotating stars scales with rotation rate according to

$$\dot{M}(\Omega) := \dot{M}(\Omega = 0) \left(\frac{1}{1 - \nu_{\text{frac}}} \right)^\xi, \quad (1.16)$$

where $\xi \approx 0.43$,

$$\nu_{\text{frac}} := \frac{\nu}{\nu_{\text{crit}}}, \quad (1.17)$$

is the ratio of the equatorial surface rotation rate to the critical (break-up) rotation rate

$$\nu_{\text{crit}}^2 := \frac{Gm}{r} (1 - \Gamma), \quad (1.18)$$

for a body with mass m at radius r . G is the gravitational constant and

$$\Gamma := \frac{\kappa L}{4\pi c G m}, \quad (1.19)$$

is the Eddington factor where κ is the opacity, L is the luminosity of the object, and c is the speed of light.

Under this prescription, the effect of rotation on mass loss for low-mass and slowly rotating stars is negligible and requires a separate prescription for mass loss without rotation.

Massive stars ($>1.3 M_\odot$) do not have convective surfaces. A convective surface is required for a strong surface magnetic dynamo. The stellar winds of massive stars do not, therefore, coupled with a magnetic field and the angular momentum loss by stellar winds is simply

$$\dot{J} = \dot{M} j_{\text{surf}} = \dot{M} \Omega(R) R^2, \quad (1.20)$$

where j_{surf} is the specific surface angular momentum, $\Omega(R)$ is the rotation rate at the surface of the star, and R is the surface radius.

Stars with convective surfaces do have a surface magnetic dynamo. Surface angular momentum loss must be treated with slightly more care. [Parker \(1958\); Schatzman \(1962\)](#) recognised that a rotating magnetised star that loses mass through ionised winds will lose more angular momentum through winds than a non-magnetised star. The enhanced spin-down results from the material in the wind having a larger specific angular momentum than the material in the star. This is because of the angular momentum contained in the stresses of the magnetic field [Weber & Davis \(1967\)](#). As the ionised wind propagates from the surface of the star, the angular momentum held in the magnetic field is transferred to the gas, removing angular momentum from the system.

One could also consider this process relative to Equation 1.20. Within that model, the specific angular momentum of the wind at the equator is $\Omega(R)R^2$. In the presence of a magnetic field, the wind torque is equivalent to what it would be if the material along

the equator was held in corotation with the surface of the star to the Alfvén radius, R_A , and then released. In this case, the angular momentum per unit mass lost in the wind in the equatorial plane is ΩR_A^2 . $R_A > R$, and as a result, angular momentum loss is enhanced.

The rate of a star's loss of angular momentum depends on several factors, including the magnetic field, wind mass loss rate, mass and radius of the star, and angular velocity. There are difficulties in relating wind torque to these factors, and many models have used a formula by Kawaler that has limitations. A more realistic formula was proposed by (Matt et al., 2012), based on 2D magnetohydrodynamic wind models that solve Alfvén surface self-consistently.

In the absence of internal angular momentum transport the spin-down rate of a star is given by

$$\frac{d\Omega}{dt} = \frac{1}{I} \left(\tau_w - \frac{dJ}{dt} \Omega \right), \quad (1.21)$$

where I is the moment of inertia of a star, $\tau_w = dJ/dt$ is the torque on the star by the stellar wind and J is the star's angular momentum.

Matt et al. (2012) prescribe the torque by winds based upon the 2D magnetohydrodynamic simulations. They find that the torque is related to the mass (M), radius (R), equatorial surface rotation rate (Ω), equatorial magnetic dipole field strength (B_{dip}) and mass loss rate (\dot{M}) of a star as

$$\tau = K_1^2 B_{\text{dip}}^{4m} \dot{M}^{1-2m} R^{4m+2} \frac{\Omega}{(K_2^2 \nu_{\text{esc}}^2 + \Omega^2 R^2)^m}, \quad (1.22)$$

where $K_1 = 1.3$, $K_2 = 0.0506$, and $m = 0.21777$ are tuned parameters obtained in their work, and ν_{esc} is the surface escape velocity ($\nu_{\text{esc}} = \sqrt{2GM/R}$).

Johnstone et al. (2015a) suggest that the dipole magnetic field strength and mass loss rate can be highly uncertain and are not well constrained by observations. They introduce a free parameter scaling to τ by setting

$$\tau_w = K_\tau \tau. \quad (1.23)$$

They found that $K_\tau = 11$ was required to match observations of the spin-down of the sun.

The use of Equation 1.22 requires a prescription of the mass loss rate and equatorial dipole magnetic field strength. Matt et al. (2012); Gallet & Bouvier (2013); Johnstone et al. (2015a) suggest that the mass loss and magnetic field strength must saturate below a certain Rossby number ($Ro = 0.1$). Observations of other magnetic activity indicators support this: coronal emission (Pizzolato et al., 2003; Wright et al., 2011; Núñez et al., 2022) as well as chromospheric diagnostics (Soderblom et al., 1993; Fang et al., 2018; Fritzevski et al., 2021).

They argue that the wind torque's dependence on rotation rate in the saturated regime must be weaker than in the unsaturated regime. They tune their angular momentum loss to open cluster rotation distribution measurements in the unsaturated regime. They find mass loss increases with increased rotation rate and decreases with mass: $\dot{M} \propto \Omega^{1.33} M^{-3.36}$. In the saturated regime \dot{M} scales with mass and takes the value of \dot{M} at the saturating Ω . They also assume that B_{dip} scales with the Rossby number and find that, in the unsaturated regime, $B_{\text{dip}} \propto (\Omega \tau_{\text{conv}})^{1.32}$, where τ_{conv} is the convective turnover timescale which varies with mass. In the saturated regime, the dipole field strength remains at the strength at the saturating Ω .

Under these assumptions, and assuming $R \propto M^{0.8}$ then the mass dependence in the unsaturated regime disappears, and the wind torque is prescribed relative to solar wind torque by

$$\tau_w = \tau_{w,\odot} \left(\frac{\Omega}{\Omega_\odot} \right)^{2.89}, \quad (1.24)$$

where $\tau_{w,\odot} = -7.15 \times 10^{30} \text{ erg s}^{-1}$ is the current solar wind torque. In the saturated regime, the mass dependence remains and is prescribed as

$$\tau_w = \tau_{w,\odot} 15^{1.89} \left(\frac{\Omega}{\Omega_\odot} \right) \left(\frac{M}{M_\odot} \right)^{4.42}. \quad (1.25)$$

Under these prescriptions, and a constant internal angular momentum transport from the core to the surface, this prescription qualitatively agrees with the rotational distributions of young clusters. The wind dependence decreases for unsaturated, slower rotating, older stars, and the rotational rate evolution is consistent with the observed Skumanich relation (Skumanich, 1972). That being said, our understanding of the evolution of stellar winds on the main sequence is still being determined, primarily because of limited knowledge about stellar winds and the wide range of rotation rates observed

at young ages. Without strong prescriptions of stellar winds, comparing observations with internal angular momentum transport models lose their informative value.

1.3.7 Summary - Effects of rotation on low-mass evolution

In this Section, we will summarise the observable features of rotation on low-mass stellar evolution. Comparative to high-mass rotating stellar evolution, the indicators of low-mass rotating stellar evolution are minimal (See [Heger et al., 2000; Maeder & Meynet, 2000](#)). The rotation rate is the main observable property of the evolution of rotation in stars. As this was discussed in length in Section 1.2 we will focus here on the impact of rotation on other observable quantities and a star's evolution.

1.3.7.1 Pre-main sequence

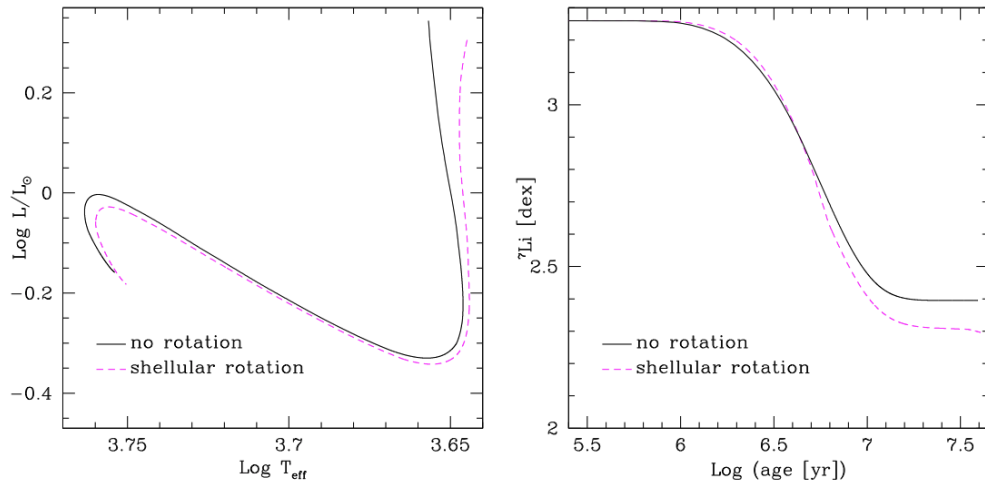


FIGURE 1.13: Left: PMS HR diagram tracks of $1 M_\odot$ solar metallicity models with and without rotation. The continuous line corresponds to a non-rotating model, while the dashed line corresponds to a rotating model with $\Omega = 20\Omega_\odot$. The tracks end when the ZAMS is reached. Right: Surface lithium abundance with time during the PMS for the same models. Sourced from Figure 1 in [Eggenberger \(2013\)](#)

Figure 1.13 (left) compares the evolutionary track of a rotating solar-type, $1M_\odot$, solar metallicity, star rotating with $20\Omega_\odot$ (twenty times the mean solar surface rotation rate) against a non-rotating model of the same mass and metallicity. Because of the introduction of the centrifugal force, the HR path is slightly shifted towards lower effective temperatures and luminosities than a non-rotating star.

During the pre-main sequence, both the changes to the rotation impact the observed lithium abundances, which are dependent on the treatment of angular momentum transport (Dumont et al., 2021). Figure 1.13 (right) displays the evolution of surface lithium abundance during the PMS phase for rotating and non-rotating models. The zero-age-main-sequence (ZAMS) surface lithium abundance of the rotating model is lower than that of the non-rotating model, indicating that including rotational effects increases lithium depletion during the PMS. However, during the beginning of the lithium depletion phase, the rotating model shows a slightly higher lithium content than the non-rotating one due to the centrifugal force lowering the temperature at the base of the convective envelope.

As the star develops a radiative zone at its centre, rotational mixing becomes the dominant factor in transporting lithium to deeper and hotter regions, where it is efficiently destroyed. This leads to a lower surface lithium abundance for the rotating model on the ZAMS compared to the non-rotating model due to the increase in differential rotation in the stellar interior during the PMS.

The duration of the disc-locking phase, which enhances differential rotation in the radiative zone, significantly impacts the sensitivity of the lithium content in rotating models. Longer disc lifetimes lead to lower surface lithium abundances on the ZAMS due to increased angular velocity gradients below the convective envelope, which enhance rotational mixing (Eggenberger et al., 2012). Moreover, as the star loses more angular momentum during the longer disc-locking phase, it reaches the ZAMS with a lower surface rotational velocity, resulting in lower lithium abundance. Therefore, a correlation between the surface velocity and lithium abundance on the ZAMS exists: stars with lower rotation rates on the ZAMS are expected to be more depleted in lithium than fast rotators on the ZAMS.

1.3.7.2 Main sequence

During the main sequence, rotational mixing begins to play a key role by changing the global stellar properties. This is illustrated in Figure 1.14 (left), which shows the main-sequence evolution for two $1 M_{\odot}$, solar metallicity models computed with and without rotation. The rotating model has an initial surface velocity of 50 km s^{-1}

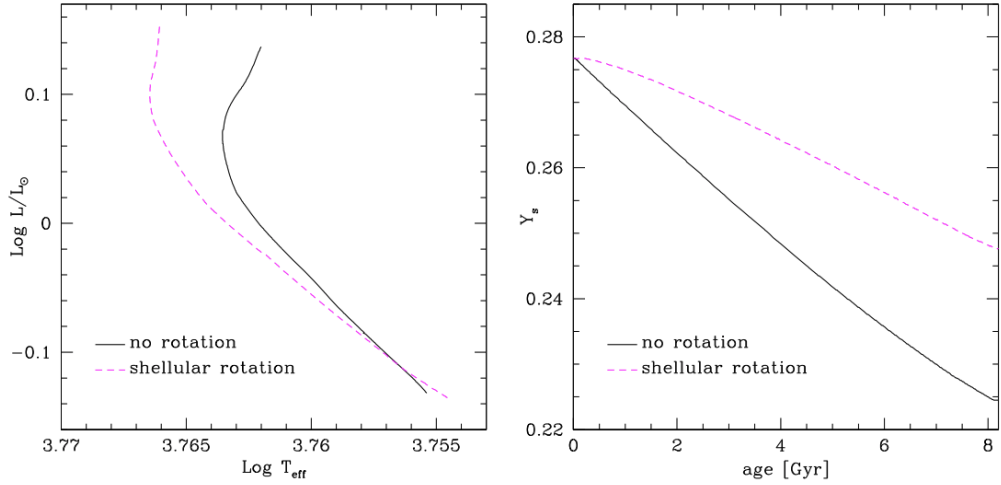


FIGURE 1.14: Left: MS HR diagram tracks of $1 M_\odot$ solar metallicity models with and without rotation. The continuous line corresponds to a non-rotating model, while the dashed line corresponds to a rotating model with ZAMS surface velocity = 50 km/s. The tracks end when the ZAMS is reached. Right: Surface helium abundance with time during the MS for the same models. Sourced from Figure 3 in Eggenberger (2013)

The rotating model is, like the PMS model, characterised by higher effective temperatures and slightly higher luminosities than the non-rotating model.

Figure 1.14 (right) highlights that the presence of rotational mixing counteracts the impact of atomic diffusion in the star’s outer layers. This leads to higher helium surface abundances for the rotating model than the non-rotating model. Consequently, the opacity in the external layers of the rotating model decreases, causing a shift towards the blue region of the HR diagram, as illustrated in Figure 1.14 (left). The differences in helium content between rotating and non-rotating stars become increasingly pronounced during the main sequence, resulting in significant distinctions in the HR diagram.

Furthermore, the inclusion of rotation affects the properties of the central layers of the star. As a result of rotational mixing, fresh hydrogen fuel is transported to the central core, leading to a higher central hydrogen mass fraction for rotating models than for models without rotation at a given age. This leads to an increase in the main-sequence lifetime.

1.3.7.3 Post-main sequence

Within the post-main sequence, the rotation effects are similar to the main sequence. When rotational effects are considered, the core helium-burning phase is shifted to higher

luminosity values. These changes are due to rotational mixing, which brings fresh hydrogen fuel into the convective core and transports helium and other H-burning products in the radiative zone.

There are no other significant enhancements in chemical abundances (See Table 2. in [Lagarde et al., 2012](#)). Rotation can, however, substantially affect the asteroseismic properties of low-mass red-giant stars [Lagarde et al. \(2012\)](#); [Eggenberger et al. \(2010\)](#). In particular, rotation decreases the derived stellar mass and increases the age. Observation and identification of non-radial oscillation modes for red giants with moderate surface rotational velocities may be complicated due to non-negligible values of rotational splitting, which can be reached depending on the assumed rotation law in the convective envelope and the star's initial velocity.

[\(Eggenberger et al., 2010; Lagarde et al., 2012\)](#) also illustrates that the HR evolution of rotating stars can be qualitatively reproduced with enhancements to the core overshooting parameter. This highlights that rotation increases the size of the convective core and changes the chemical composition of the radiative zone.

1.4 Todo

Write section on ways that observations of rotation are made - precise techniques.

- Rotation period from light curves - acf method and periodogram
- Doppler broadening spectroscopy
- Asteroseismic inference of rotation rate - OLA techniques + Forward modelling

Chapter 2

The Intermediate Period Gap

Abstract

Photometric variability due to stellar spots allows astronomers to measure the surface rotation periods of stars. Within multiple missions' rotational period samples (e.g. *Kepler*, *K2*, *ZTF*) there is a distinct dearth of observations of stars rotating at intermediate periods $15 \gtrsim P_{rot} \gtrsim 20$ days. This dearth of observations is known as the intermediate period gap. The position of this gap varies with the colour of the stars. Various mechanisms have been proposed to explain the dearth of observations from stars physically "jumping" the gap through enhanced wind-braking, to stars above and below the gap representing two populations of stars, to the gap representing a minima of probability to observe rotation rate. The exact cause of the dearth of observations is currently unknown. In this Chapter we discuss the various hypotheses of the mechanism underlying the intermediate period gap and discuss our work to determine the likelihood of each of these mechanisms being at play.

2.1 Introduction

Measurement of the rotational period of samples of stars allows us to understand internal mechanisms that we otherwise would not be able to probe. For example, the mass-dependent core-envelope coupling and decoupling of young stars have only recently been observed by measuring the rotational period of stars with age through the rotational period distribution of clusters (Reinhold & Gizon, 2015). An unexplained feature of the rotational period distribution of low-mass main-sequence stars comes in the form of what is known as the intermediate period gap. The intermediate period gap represents a minimum of observations of stars with particular rotation periods dependent on temperature, first observed by McQuillan et al. (2014). The period that the gap appears increases with decreasing temperature/mass. The gap is robust between different photometric observation missions (McQuillan et al., 2014; Davenport, 2017; Davenport & Covey, 2018; Lu et al., 2022), multiple period detection methods and varies its position in period with respect to mass. This suggests that the lack of observation of stars is not a quirk in the data or the data analysis process but a physical feature of the stars we are observing.

Multiple mechanisms have been proposed to explain the intermediate period gap. McQuillan et al. (2014) first proposed that the gap represents bimodal bursty star formation in the local *Kepler* field. They suggest that the lower rotation period (faster rotators) prong represents a younger population and the upper rotation period prong represents an older population, with the gap representing a minima in star formation at a particular time. Davenport & Covey (2018) support local bursty star formation hypothesis by separating the *Kepler* rotation period distribution by distance through *Gaia* parallaxes. They find that the gap appears to disappear for stars further away than 525 pc. They fail to acknowledge, however, that at those distances (a) observations of stars is magnitude-limited to brighter high-mass stars ($M > 0.9 M_{\odot}$) where observations of the gap are tentative and (b) period detection and temperature/colour measurement are much less precise. If the gap extends up to these high-mass stars, then its existence can be blurred out by the imprecision of these measurements. Their work may also support this explanation. In the full (McQuillan et al., 2014) sample the gap disappears for high mass ($M_{\odot} > 0.8$, $B_P - R_P < 1.0$) stars. In the distance limited (< 525 pc) sample, the gap appears to permeate to these higher-mass stars. This can be seen in

the rotational period-colour distribution in the top two panels in Figure 2 of [Davenport & Covey \(2018\)](#) where distance is limited to 525pc.

More recent works significantly disfavour the bursty star formation hypothesis. [Gordon et al. \(2021\)](#) detected the gap in multiple pointings of the *K2* mission, while [Curtis et al. \(2020\)](#) found that the open cluster Ruprecht 147 contains stars above and below the gap - and the possible detection of a star within the intermediate period gap. This suggests that the gap is not a coeval feature and rather a feature of the rotational evolution of low-mass stars. [Curtis et al. \(2020\)](#) instead proposed that the gap aligns with a line of constant Rossby number ($R_o \sim 0.6$) - rotation rate scaled quantity shown to be associated with the magnetic activity of stars.

[\(McQuillan et al., 2014\)](#) suggested another explanation for the intermediate period gap through a rapid spin-down - "jumping" across the gap quickly, resulting in decreased stars' density in this period-colour space region. For example, the rapid spin-down could be caused by core and convective envelope rotational decoupling at the upper edge of the lower prong near the rotational period gap. In this mechanism, the core and envelope evolve independently; the envelope - having a much smaller moment of inertia than the core - is spun down rapidly under the same magnetic braking conditions. Following the gap the core and envelope then recouple, exchanging angular momentum and returning to a normal rate of magnetic braking. [Gordon et al. \(2021\)](#) argued in favour of this hypothesis based on the rotation period distribution of *K2*. [Curtis et al. \(2020\)](#) argued that two-zone angular momentum transport models, such as those by [Spada & Lanza \(2020\)](#) can reproduce a stalled braking behaviour required to explain the lower prong of the intermediate rotational period gap - but their model could not explain the rapid-spin down. This hypothesis is generally supported by the tentative observation of low-mass fully convective stars permeating the gap ([Lu et al., 2022](#)).

[Santos et al. \(2021\)](#) measured the rotation period of stars with lower variability and expanded the upper range of rotation periods that can be observed through *Kepler* data. They did not find more stars in or around the intermediate period gap than [McQuillan et al. \(2014\)](#), suggesting that the gap is, in fact, empty. [Lu et al. \(2022\)](#) examined the kinematic stellar ages below and above the gap. They tentatively found that the relation between kinematic age and Rossby number of stars above and below the gap is discontinuous (see Figure 11 in their work). While this result supports the

hypothesis that stars could have gone through a phase of rapid spin-down and jumped over the gap, more precise measurement of kinematic ages for more stars is required to support this claim.

On the other hand, Reinhold et al. (2019) and Reinhold & Hekker (2020) proposed that a transition from dark spot creates the gap - to bright facula dominance in the activity cycle of a star. In this work, they differentiate between the rotation brightness modulation and brightness modulation from the stellar activity cycle. Stellar activity modulation refers to the long-term evolution of average brightness due to stellar spots and faculae rather than variations on the rotational time scale. They suggest that as a star spins down and the magnetic field topology changes, the initially strong and long-lived spots are replaced by smaller, short-lived spots surrounded by bright faculae. In such a scenario, the photometric variability amplitude decreases in because of the partial cancellation by the increase and decrease in brightness from the faculae and spots, respectively. Hence, the stars with small photometric variability will not be detected. This hypothesis is supported by the gap aligning with a line of constant Rossby number - indicative of common magnetic field evolution between these stars - and by the photometric variability reaching a local minimum surrounding the gap. The authors do not appear to suggest a reason for spot-dominated stars appearing above the gap nor a mechanism for the increase in rotational photometric variation amplitude above the gap. Further, the variability levels on both sides of the gap are not close to the detection limit: periods are detected for stars with similar properties at much lower R_{per} values.

If the gap aligned itself with a line of constant rotation in only one mission, then the mechanism underlying the gap could be more readily explained through the selection function of said mission. These factors suggest that the intermediate period gap represents a function of stellar evolution or an unaccounted-for problem in observing rotation periods through photometric oscillations from stellar spots. The intermediate period gap interests astronomers and astrophysicists because the mechanism underlying it is unexplained. Therefore, the effects of this process are unknown in stellar evolution. There are two broad categories we can separate explanations for the gap into. First, consider that the intermediate rotational period gap represents a sudden onset of extreme rotational braking. Proceeding the gap, there is an overabundance of rotational period observations. The overabundance has been suggested to represent a period of

core envelope recoupling. The loss in angular momentum from surface rotational braking is counteracted by the core-to-envelope angular momentum transport - resulting in a longer period of evolution spent at these rotational periods. In this model, at some point, the core and surface again decouple, and rotational braking is so strong over a short period in evolution that very few stars are observed at these rotational periods. While most models of angular momentum transport can explain the decoupling through the decreased angular momentum gradient between the core and the surface (), the cause of the strong braking within the gap is not so easily explained, but it is not without motivation. Young stars - stars below the lower branch in period space - sparsely populate rotational period distribution although they are rotating quickly and have strong magnetic fields (meaning there is a very high probability of observing the rotational periods of these stars). On the other hand, because they rotate quickly and have strong magnetic fields, they undergo strong magnetic wind braking and quickly evolve through this regime. The sparsity of their observation then results from their quick transition through this regime. Magnetic braking is proportional to the star's rotational rate, the strength of the underlying magnetic field, and the mass loss (which depend on the rotational rate). Suppose this is the correct model of the rotational evolution near the gap. In that case, gap stars represent a laboratory for understanding the evolution of the magnetism in stars, and the underlying mechanism that provides the enhanced wind braking is of interest to the scientific community. This enhanced braking would need to be accounted for in gyrochronological models.

On the other hand, let's say that the stars within the gap exist; there are stars with rotational periods that would place them in the gap, but we cannot measure their periods for whatever reason. If this is the case, we have undoubtedly observed gap stars that we do not know are gap stars. Therefore, whether gap stars are peculiar - photometrically, spectroscopically or asteroseismically - is unknown. It is entirely possible, but likely not probable, that gap stars have been previously flagged as peculiar, but the link between the gap and these stars has never been made. On the other hand, gap stars may not be otherwise peculiar - chemically or, say, in terms of magnetic activity. If indeed they are not otherwise peculiar, then, oxymoronically, the reason for their lack of observation raises more questions about the mechanism underlying the gap.

2.1.1 Stellar activity indicators

Stellar magnetism is a complex component of stellar evolution that is hard to model. Links between magnetism and mass, metallicity, age, convection, and rotation have been identified (Cao & Pinsonneault, 2022). These links are, however, based upon observations of stars rather than astrophysical theory. The observation of rotational modulation in a light curve, and the observation of surface rotation from that modulation, requires cool spots created by concentrated magnetic fields near the surface of a star. Stars with stronger magnetic fields tend to express larger spot coverage, thus having larger rotational photometric modulation and more readily observable rotation periods.

Stellar activity is the collective term used to describe different effects magnetic fields have on stars. This name arises from the variability phenomena arising from structured magnetic fields emerging from the convective envelope of stars - e.g. flares and photometric variability from stellar spots. The strength of the magnetic field can be directly or indirectly measured in a number of ways.

Throughout the stellar atmosphere, emission features arise through the interaction of light and elements. Different absorption features arise from both different elements and different stellar atmosphere conditions. Flux through the Ca II H and K lines correlate with the magnetic field strength within the chromosphere and is therefore commonly used as an indicator of activity for cool main-sequence stars.

Two measures of the chromospheric Ca II H and K line fluxes are generally adopted. First through the classical S index. This is the flux ratio in the core of the Ca II H and K lines to close by continuous windows. Scaling factors are generally introduced between telescopes, as the ratio of these fluxes can depend on a given telescope's efficiency and the relative exposure times in these spectral windows. The quantity S is sensitive to the integrated emission over these windows and the photospheric radiation transmitted in the H and K passbands. The quantity R_{HK}^+ eliminates this contribution and is thus a more reliable measure of the chromospheric Ca II H and K flux - therefore more accurately reflecting the magnetic field strength of stars.

Another indirect measure of the magnetic field's strength arises from the stars photometric variability. Stars that have stronger magnetic fields generally express more stellar spots. A star that expresses stellar spots results in larger photometric variability as a

star rotates. Photometric variability can be measured through various means. The first is the amplitude of periodic variability, R_{per} . This is defined as the median of the range between the 5th and 95th percentile of normalised flux in bins of the light-curve divided into sections of the length of the measured rotational period (McQuillan et al., 2014). Larger R_{per} stars are expected to have more easily detectable rotation periods because the larger the star's variability as it rotates, the more easily distinguishable this variability is from noise.

Finally, the most recent measure of stellar activity has arisen from the measurement of the fractional spot coverage of stars (See Chapter ?? and (Cao & Pinsonneault, 2022)). They found that fitting APOGEE spectra with two temperature components allows one to infer the surface fractional spot coverage and the temperature contrast of the spots to the ambient surroundings. The stellar spot expression of stars is expected to be tied to the photometric variability of those stars with larger photometric variability arising from a larger fractional spot coverage.

All of these measurements of magnetic activity have been shown to be related to each other and follow similar relations with the stellar Rossby number. Magnetic activity tends to saturate below a $R_o < 0.3$ (Cao & Pinsonneault, 2022) (fast rotation) and decrease with a power law as R_o increases. This relation reflects the decreased probability of observing older slow-rotating stars in the McQuillan et al. (2014) sample. Variations to magnetic activity can therefore indicate variations to the expression of stellar spots and, thus, the observability of stellar rotation.

The magnetic activity also varies with the stellar magnetic cycle of a star, with some scatter to magnetic activity indicators being attributed to this. Therefore, a single temporal measurement of magnetic activity must be treated with care. In this work we will adopt a population study approach to minimise this effect.

2.2 The decrease in photometric variability of stars near the intermediate period gap

The first mechanism we consider is that the rotation period gap reflects a decrease in photometric variability due to a variation in the magnetic field strength of stars near

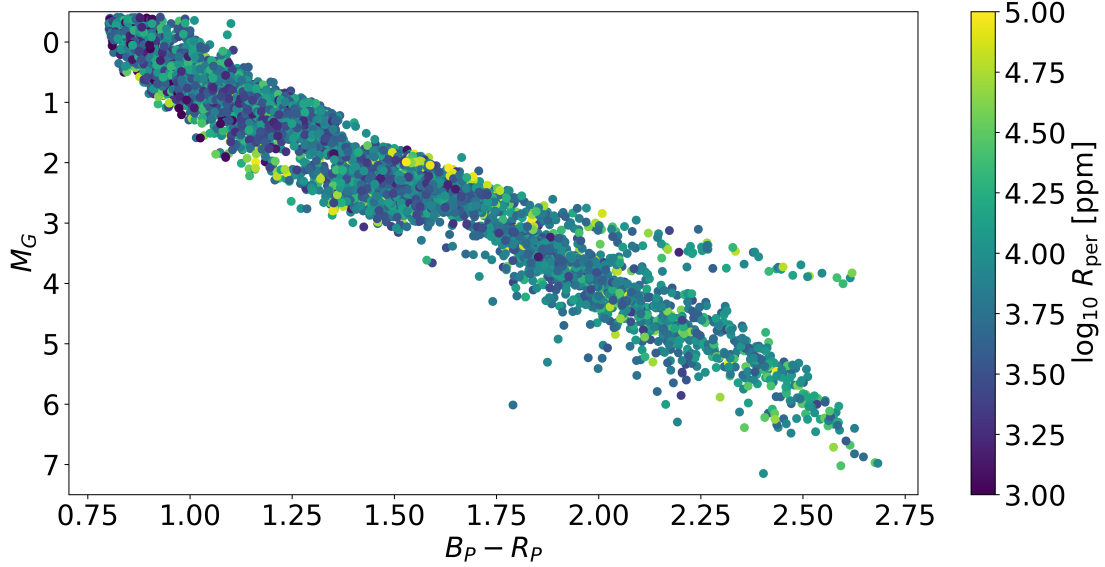


FIGURE 2.1: HR diagram of the closeby rotating main-sequence sample colours by photometric variability (R_{per}).

the gap. We will begin with the 33,000 stars with rotation periods from [McQuillan et al. \(2014\)](#). All stars in this sample lay within the cross-match with Gaia data release 3, which contains precise measurements of the $B_P - R_p$ colour, G -band magnitude and distance from parallax. We limit our sample to stars within the nearest 525pc, motivated by the results of [Davenport & Covey \(2018\)](#). While this reduces the sample to 8,594 stars it ensures that the measured $B_P - R_P$ and rotation periods are as accurate as possible. We made cuts in Gaia DR3 magnitudes and colours using $M_G > 0$ and $B_P - R_P > 0.8$ to target below the main-sequence turnoff and stars lower mass than the Kraft Break. This leaves us with a sample of 6,243 nearby stars with reliable surface rotation and colour measurements. These stars are shown in Figures 2.1 and 2.2 where we have plotted them as a HR diagram and log rotation period against $B_P - R_P$ colour. In Figure 2.2 the decrease in photometric variability surrounding the gap can be clearly seen.

From this sample we can establish a description of the average evolution of photometric variability around the intermediate period gap. We will first separate the subsample into bins of $B_P - R_P$ (colour) from 0.8-2.5 of size 0.17 (10 bins). In each colour interval, we then split the data into *log* rotational period intervals of width 0.07 dex between 0.4 and 1.8 dex - which correspond to 2.5 and 70 days, respectively. We then compute the median and median absolute deviation of R_{per} in each colour and rotational period bin. The median is used here to attempt to alleviate the effect of activity cycles on the variance on the magnetic activity and the median absolute deviation establishes the

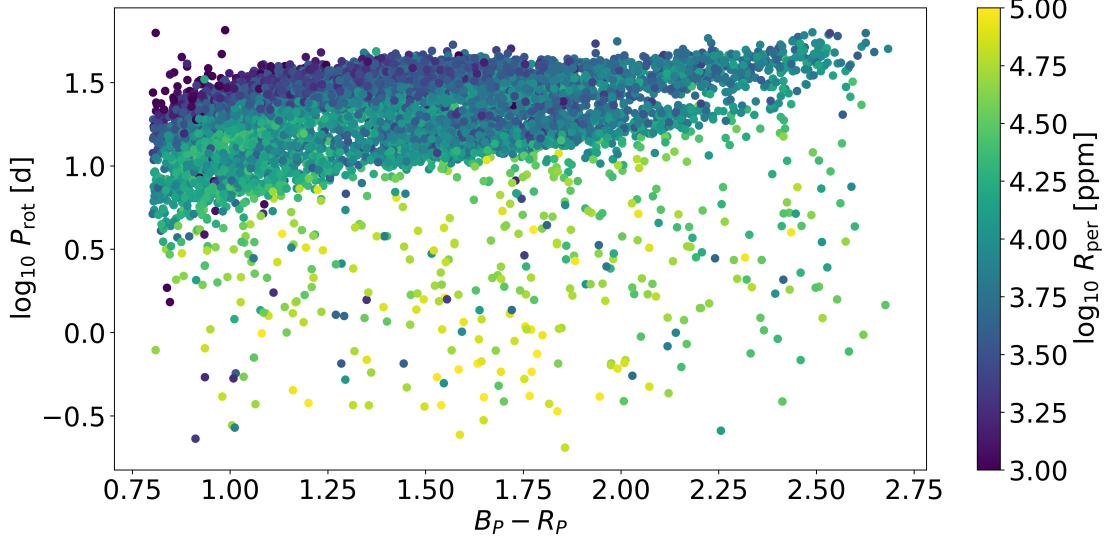


FIGURE 2.2: \log_{10} of the rotation period against $GaiaB_P - R_P$ colour of the closeby rotating main-sequence sample colours by photometric variability (R_{per}). In this Figure we can see clearly see the decrease in photometric variability of stars near the gap.

scatter on the measured photometric variability - regions with large median absolute deviation should be treated as less reliable measurements. We neglected the regions with few stars (<5). This removes the spurious stars that have not ascended onto the lower prong of the intermediate period gap, which do not indicate large-scale trends in the data. We reconfirm that R_{per} tends to increase with mass, decrease with the rotational period, and decrease towards the rotational period gap (Reinhold & Hekker, 2020; Santos et al., 2021). Comparing Figures 2.2 and 2.3, we also confirm that the gap aligns itself with a minima in R_{per} .

As a result of the large-scale variability with stellar mass and rotational period, the position of the minima becomes harder to notice as $B_P - R_P$ approaches 0.8. To make the minima more prominent, we plot the same data in Figure 2.4. We show the median R_{per} (scatter points) and scatter (errorbars) against the \log_{10} of the rotation period for each colour range indicated in brackets - here, the colour of the interval increases down the plot - as well as fitted cubic spline to the data (dashed). From the cubic spline, we can use the first and second derivatives of the spline to accurately determine the position of the local minima in R_{per} , which is indicated by the solid vertical blue line. The calculation of the position of the minima is an automated process. We first find where the first derivative is close to zero and where the second derivative is relatively large and greater than zero - this is to ensure we ignore any spurious jitter in the spline fit. We use an automated process ensure we have not selected a position that we believe

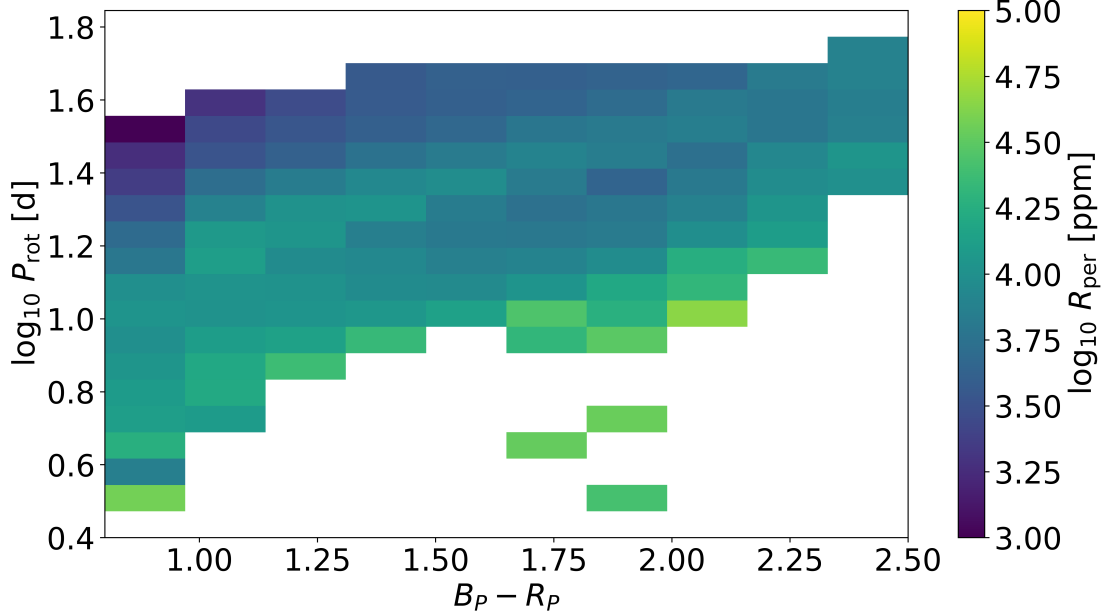


FIGURE 2.3: 2D binned photometric variability (R_{per}) for the slices of \log_{10} of the rotation period and colour $GaiaB_P - R_P$ used in this work. Comparing this Figure and 2.2 the alignment of the minima of photometric variability and observation of stars in the gap can be seen.

aligns with the intermediate period gap though the resulting position of minima can vary slightly depending on the smoothing of the cubic spline. The first minima, in regards to the rotational period, in the $B_P - R_P$ (0.8-0.97) bin was manually ignored. The position of the minima are shown in blue in Figure 2.5, where it is clear that the majority of minima align with the intermediate period gap. We note that the minima do not accurately predict the position of the intermediate period gap for $B_P - R_P > 2.16$. We believe this is because of the small number of stars below the gap in this colour range which were cut due to them not containing enough stars. With larger numbers of observations of low-mass stars below the gap we believe our prediction of the position of the rotation period gap with R_{per} would be more accurate in this regime. We also note that the average photometric modulation amplitude tends to peak to a maximum with a larger R_{per} than stars on the lower prong of the rotational period gap despite having longer rotation periods. Whether this peak is indicative of stronger photometric activity suddenly above the gap or of suppression of photometric activity below the gap is unknown.

A possible explanation for the decrease in median photometric variability comes from the nature of the dearth of observations itself. The gap is not horizontally aligned and increases in period for stars of lower mass (higher $B_P - R_P$). R_{per} generally decreases

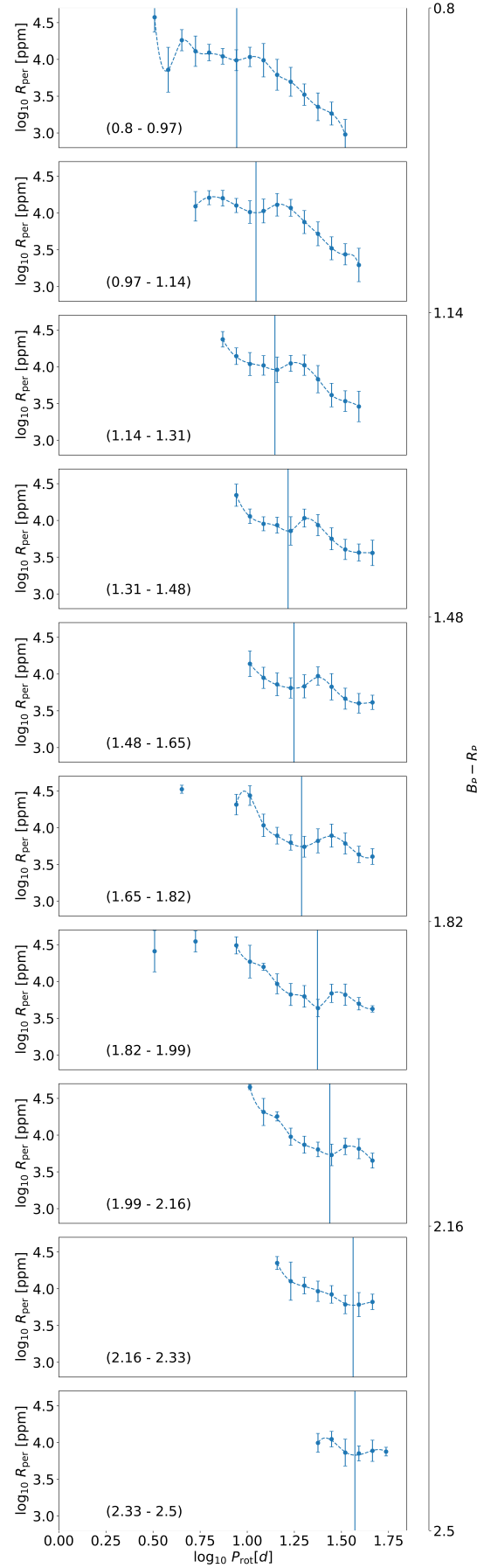


FIGURE 2.4: Median and median absolute deviation of photometric variability (R_{per}) against \log_{10} of the rotation period in bins of and colour $Gaia B_P - R_P$ (indicated in brackets). Here we have fitted a cubic spline to median R_{per} and calculated minima using the first and second derivatives of the fitted cubic spline. The minima here are shown by solid vertical blue lines. These minima align with the rotational period gap.

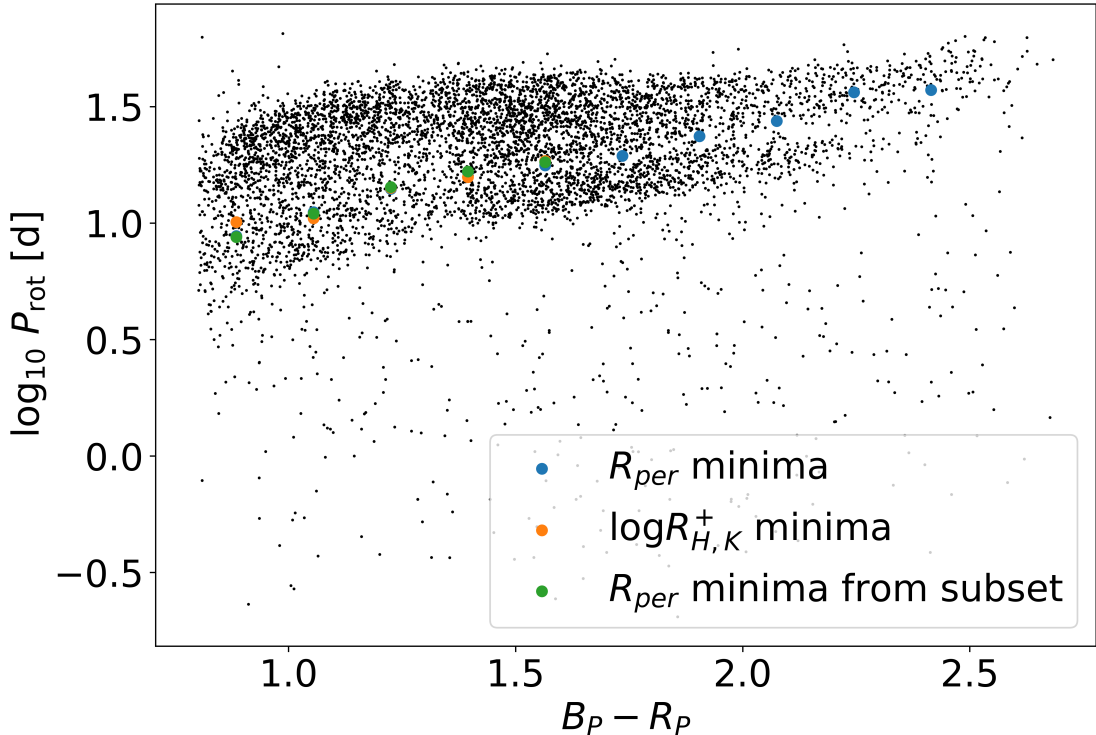


FIGURE 2.5: The position of the identified minima in R_{per} against rotational period using the full close-by rotating main-sequence Kepler sample, the R_{per} minima identified with the Kepler LAMOST cross-match and the $\log_{10} R_{H,K}^+$ minima identified with the Kepler LAMOST cross-match.

with mass and rotation period. Taking the median value in slices of constant rotation period near the dearth of observations will be systematically biased in different ways as it passes through the dearth. In order of increasing rotation period, the slice will contain: (1) majority fast rotating but redder stars and a small number of slow-rotating bluer stars, (2) approximately equal fast-rotating red stars and slow-rotating blue stars, and finally (3) majority slow-rotating bluer stars and a small number of fast-rotating redder stars. The relationship between the R_{per} , mass and rotation period are not easily parameterised - especially near the gap. However, we can confirm that this effect does not skew our results by calculating the median and median absolute deviation of $B_P - R_P$ in each colour and rotational period bin. We have shown this in Figure ???. We confirm that the minima and maxima of R_{per} with rotation period in each colour bin do not correspond to a minima or maxima in colour that would indicate that this effect is at play. The variation in R_{per} is, therefore, a physical effect that aligns itself with the rotational period gap.

While it has been well established that the photometric variability of stars decreases

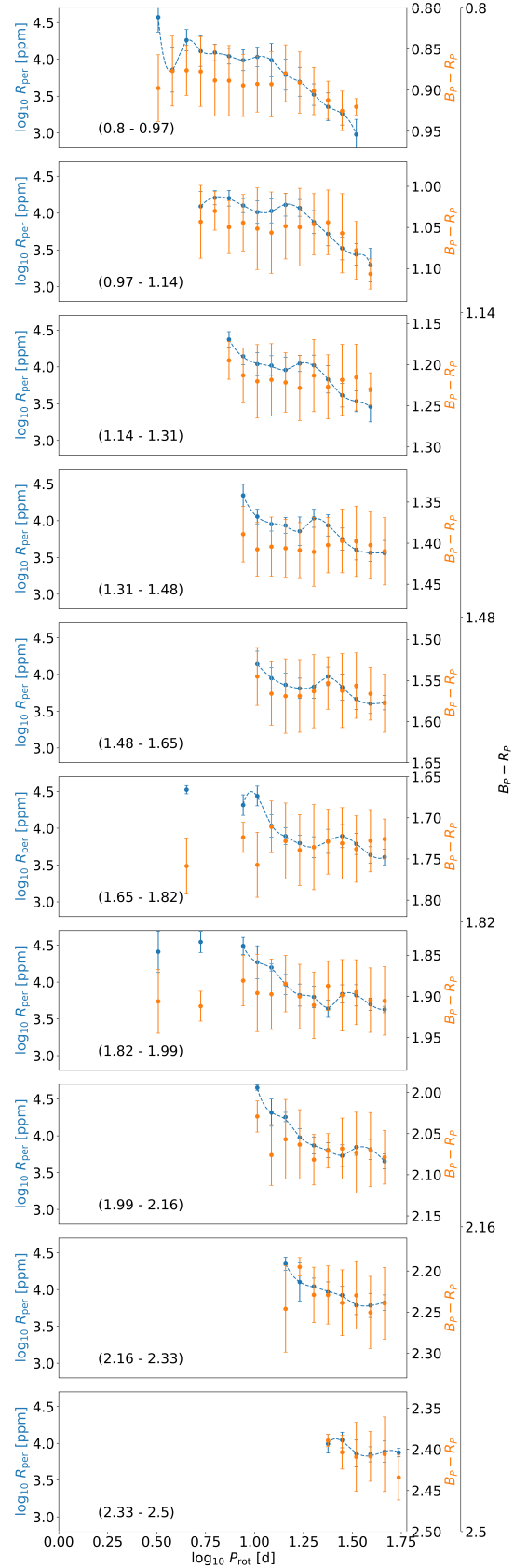


FIGURE 2.6: Median and median absolute deviation of photometric variability (R_{per}) (blue) and $B_P - R_P$ (orange) against \log_{10} of the rotation period in bins of $Gaia$ $B_P - R_P$ colour (indicated in brackets). The position of the minima in R_{per} do not align with a maxima or minima in $B_P - R_P$ implying that the colour bias when fitting across the dearth can be the cause of the R_{per} minima.

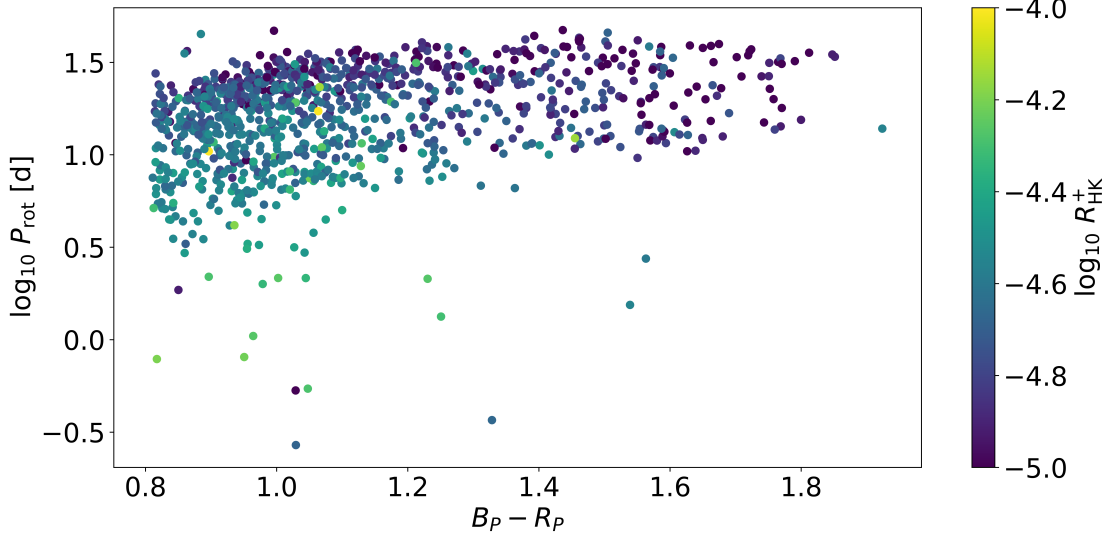


FIGURE 2.7: The LAMOST chromospherically active and *Kepler* rotating closeby, main-sequence cross-match \log_{10} of rotational period $\log_{10} P_{\text{rot}}$ against $Gaia B_P - R_P$ colour coloured by $\log_{10} R_{\text{HK}}^+$. It is unclear from this whether $\log_{10} R_{\text{HK}}^+$ decreases toward the gap like R_{per} .

towards the intermediate period gap other magnetic activity indicators have not been explored in this regard only the large scale trends with stellar mass and rotation. Suppose other magnetic activity indicators vary in the same fashion as R_{per} . In that case, it is more likely that the decrease in R_{per} towards the gap results from a variation in the magnetic field of stars. [Zhang et al. \(2020\)](#) extracted the chromospheric magnetic activity indexes, S and $\log R_{\text{HK}}^+$, for 59,816 stars from low-resolution LAMOST spectra in the LAMOST-Kepler program. The cross-match of their work with the nearby rotating main sequence we established yielded 1060 stars. The stars in the cross-match tend to be the higher mass, brighter, stars with $B_P - R_P < 1.8$, where the intermediate period gap is less apparent. Given that we could predict the position of the gap for these stars in our earlier experiment, we carry forward and re-analyse their data under a new framework.

$\log R_{\text{HK}}^+$ provides a more accurate measure of the chromospheric magnetic activity than S , which is uncoupled from a radiative contribution, so we adopt $\log R_{\text{HK}}^+$ in this work. The resulting rotational distribution of stars are shown in Figure 2.7 coloured by $\log R_{\text{HK}}^+$. Due to the smaller number of stars and lower precision of $\log R_{\text{HK}}^+$ than R_{per} it is not clear whether $\log R_{\text{HK}}^+$, like R_{per} decreases towards to the intermediate period gap.

To determine this more concretely, we adopt the same process as we described earlier

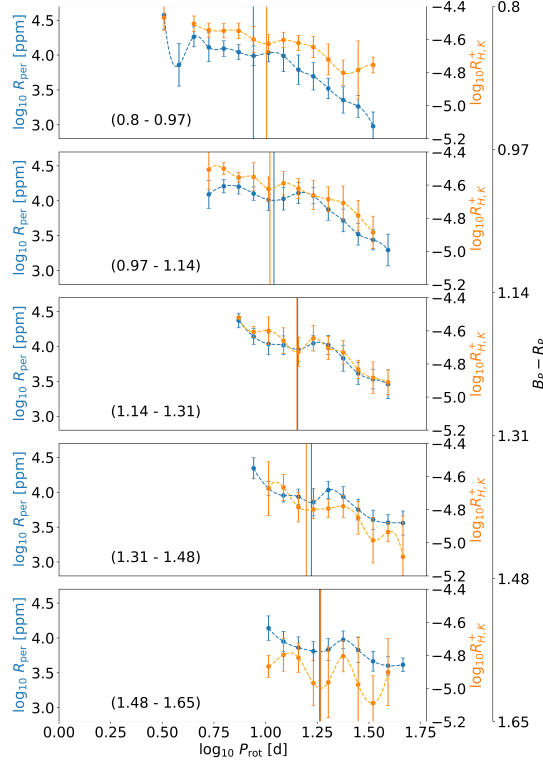


FIGURE 2.8: Median and median absolute deviation of photometric variability (R_{per}) (blue) and LAMOST $\log_{10} R_{\text{HK}}^+$ against \log_{10} of the rotation period in bins of and colour *Gaia* $B_P - R_P$ (indicated in brackets). Here we have fitted a cubic spline to median of these values in each bin and calculated minima using the first and second derivatives of the fitted cubic spline. The minima in R_{per} are shown by solid vertical blue lines while the minima in $\log_{10} R_{\text{HK}}^+$ are shown in solid vertical orange lines. These minima align with each other and the rotational period gap.

to find the minima in R_{per} in a bin of colour against the rotational period. We again separate the stars into the same slices of $B_P - R_P$ and log of rotation period and remove any bins containing small numbers of stars (<2). This cut-off was chosen because of the reduced number of stars in the sample but the results should therefore be treated with more caution because we are relying on small number statistics. The median and median absolute deviation of both $\log R_{\text{HK}}^+$ and R_{per} in these slices was then calculated, which we then fit with cubic splines against the log of rotation period. We have repeated this method on R_{per} here because we are using a subset of the original stars and to compare the recovered minima from the subset more accurately - this also allows us to confirm the accuracy of the fit of our minima in the first test. The minima of the cubic spline fits are then calculated again using the first and second derivatives. Due to the smaller number of stars in the sample, we have ignored minima that align with bins with less than four stars. Because of this we have manually ignored the low-rotational period $\log R_{\text{HK}}^+$ minima in the $B_P - R_P = (0.97 - 1.14)$ and $(1.14 - 1.31)$ slices.

We compare the distributions of R_{per} and $\log R_{HK}^+$ against the log of rotation period in Figure 2.8 and show the found minima in blue and orange solid vertical lines for R_{per} and $\log R_{HK}^+$ respectively. Like photometric variability, $\log R_{HK}^+$ tends to decrease with rotational period - owing to their relation to the strength of the magnetic field.

We show the comparison of the recovered minima from R_{per} using this subset as well as the minima recovered using $\log R_{HK}^+$ in Figure 2.5. The recovered R_{per} minima using the subset lay on top of the R_{per} minima recovered using the full sample. Interestingly, we may detect previously unreported minima in $\log R_{HK}^+$ close to the rotation period gap.

Excluding the minima recovered in the $B_P - R_P$ - (0.8-0.97) bins the minima that we recover in $\log R_{HK}^+$ against logged rotational period are in the same period bin and are close in position to the minima of R_{per} we recover, which we have established aligns with the intermediate period gap. The alignment of the minima is also robust to variation to smoothness of the fitted cubic spline - suggesting that the minima are not spurious.

Measurements of $\log R_{HK}^+$ are less precise than R_{per} , which is reflected in the relatively larger median absolute deviation. The detection of the coincidence in a single slice of $B_P - R_P$ could be explained through this imprecision. However, the detection of this in multiple slices of $B_P - R_P$ suggests that the cause of the minima is related. We suggest that further study of this relationship is required to confirm the coincidence of the minima with a larger dataset of chromospheric magnetic activity indicators or with other magnetic activity indicators.

Bibliography

- Affer L., Micela G., Favata F., Flaccomio E., Bouvier J., 2013, [Monthly Notices of the Royal Astronomical Society](#), 430, 1433
- Ahlborn F., Bellinger E. P., Hekker S., Basu S., Angelou G. C., 2020, [Astronomy & Astrophysics](#), 639, A98
- Albrecht S., Winn J. N., Carter J. A., Snellen I. A. G., de Mooij E. J. W., 2011, [The Astrophysical Journal](#), 726, 68
- Albrecht S., Setiawan J., Torres G., Fabrycky D. C., Winn J. N., 2013, [The Astrophysical Journal](#), 767, 32
- Amard L., Palacios A., Charbonnel C., Gallet F., Georgy C., Lagarde N., Siess L., 2019, [Astronomy & Astrophysics](#), 631, A77
- Angus R., et al., 2020, [The Astronomical Journal](#), 160, 90
- Arlt R., Hollerbach R., Rüdiger G., 2003, [Astronomy & Astrophysics](#), 401, 1087
- Augustson K. C., Brun A. S., Toomre J., 2019, [The Astrophysical Journal](#), 876, 83
- Balbus S., Hawley J., 1994, [Monthly Notices of The Royal Astronomical Society - MON NOTIC ROY ASTRON SOC](#), 266
- Barker A. J., Jones C. A., Tobias S. M., 2019, [Monthly Notices of the Royal Astronomical Society](#), 487, 1777
- Barker A. J., Jones C. A., Tobias S. M., 2020, [Monthly Notices of the Royal Astronomical Society](#), 495, 1468
- Beck P. G., et al., 2011, [Science](#), 332, 205
- Beck P. G., et al., 2012, [Nature](#), 481, 55

- Bedding T. R., et al., 2011, *Nature*, 471, 608
- Belkacem K., et al., 2015, *Astronomy & Astrophysics*, 579, A31
- Borucki W. J., et al., 2010, *Science*, 327, 977
- Cantiello M., Mankovich C., Bildsten L., Christensen-Dalsgaard J., Paxton B., 2014, *The Astrophysical Journal*, 788, 93
- Cao L., Pinsonneault M. H., 2022, *Monthly Notices of the Royal Astronomical Society*, 517, 2165
- Cao L., Pinsonneault M. H., van Saders J. L., 2023, Core-envelope decoupling drives radial shear dynamos in cool stars, <http://arxiv.org/abs/2301.07716>
- Ceillier T., et al., 2017, *Astronomy & Astrophysics*, 605, A111
- Chaboyer B., Zahn J.-P., 1992, *Astronomy and Astrophysics*, 253, 173
- Charbonnel C., Talon S., 2005, *Science*, 309, 2189
- Charbonnel C., Talon S., 2008,] 10.1017/S1743921308022710, 252, 163
- Charbonnel C., Vauclair S., Maeder A., Meynet G., Schaller G., 1994, *Astronomy and Astrophysics*, 283, 155
- Curtis J. L., Agüeros M. A., Douglas S. T., Meibom S., 2019, *The Astrophysical Journal*, 879, 49
- Curtis J. L., et al., 2020, *The Astrophysical Journal*, 904, 140
- Davenport J. R. A., 2017, *The Astrophysical Journal*, 835, 16
- Davenport J. R. A., Covey K. R., 2018, *The Astrophysical Journal*, 868, 151
- David T. J., Angus R., Curtis J. L., van Saders J. L., Colman I. L., Contardo G., Lu Y., Zinn J. C., 2022, *The Astrophysical Journal*, 933, 114
- Deheuvels S., et al., 2014, *Astronomy and Astrophysics*, 564, A27
- Deheuvels S., Ballot J., Beck P. G., Mosser B., Østensen R., García R. A., Goupil M. J., 2015, *Astronomy & Astrophysics*, 580, A96

- Deheuvels S., Ballot J., Eggenberger P., Spada F., Noll A., Hartogh J. W. d., 2020, *Astronomy & Astrophysics*, 641, A117
- Delorme P., Collier Cameron A., Hebb L., Rostron J., Lister T. A., Norton A. J., Pollacco D., West R. G., 2011, *Monthly Notices of the Royal Astronomical Society*, 413, 2218
- Denissenkov P. A., Pinsonneault M., Terndrup D. M., Newsham G., 2010, *The Astrophysical Journal*, 716, 1269
- Distefano E., Lanzafame A. C., Lanza A. F., Messina S., Korn A. J., Eriksson K., Cuypers J., 2012, *Monthly Notices of the Royal Astronomical Society*, 421, 2774
- Distefano E., et al., 2022, Gaia Data Release 3. Rotational modulation and patterns of colour variations in solar-like variables, <http://arxiv.org/abs/2206.05500>
- Douglas S. T., Agüeros M. A., Covey K. R., Kraus A. L., 2017, *The Astrophysical Journal*, 842, 83
- Douglas S. T., Curtis J. L., Agüeros M. A., Cargile P. A., Brewer J. M., Meibom S., Jansen T., 2019, *The Astrophysical Journal*, 879, 100
- Dumont T., Palacios A., Charbonnel C., Richard O., Amard L., Augustson K., Mathis S., 2021, *Astronomy & Astrophysics*, 646, A48
- Eddington A. S., 1918, *The Astrophysical Journal*, 48, 205
- Eddington A. S., 1925, *The Observatory*, 48, 73
- Eddington A. S., 1926, *The Internal Constitution of the Stars*. <https://ui.adsabs.harvard.edu/abs/1926ics..book.....E>
- Eddington A. S., 1929, *Monthly Notices of the Royal Astronomical Society*, 90, 54
- Eggenberger P., 2013, *EPJ Web of Conferences*, 43, 01005
- Eggenberger P., Meynet G., Maeder A., Hirschi R., Charbonnel C., Talon S., Ekström S., 2008, *Astrophysics and Space Science*, 316, 43
- Eggenberger P., Miglio A., Montalban J., Moreira O., Noels A., Meynet G., Maeder A., 2010, *Astronomy and Astrophysics*, 509, A72
- Eggenberger P., Montalbán J., Miglio A., 2012, *Astronomy & Astrophysics*, 544, L4

- Eggenberger P., et al., 2019, [Astronomy & Astrophysics](#), 621, A66
- Elvey C. T., 1929, [The Astrophysical Journal](#), 70, 141
- Endal A. S., Sofia S., 1978, [The Astrophysical Journal](#), 220, 279
- Fang X.-S., Zhao G., Zhao J.-K., Bharat Kumar Y., 2018, [Monthly Notices of the Royal Astronomical Society](#), 476, 908
- Fellay L., Buldgen G., Eggenberger P., Khan S., Salmon S. J. A. J., Miglio A., Montalbán J., 2021, [Astronomy & Astrophysics](#), 654, A133
- Fricke K., 1967, [Science](#), 156, 1101
- Friend D. B., Abbott D. C., 1986, [The Astrophysical Journal](#), 311, 701
- Fritzewski D. J., Barnes S. A., James D. J., Järvinen S. P., Strassmeier K. G., 2021, [Astronomy & Astrophysics](#), 656, A103
- Fuller J., Cantiello M., Stello D., Garcia R. A., Bildsten L., 2015, [Science](#), 350, 423
- Fuller J., Piro A. L., Jermyn A. S., 2019, [Monthly Notices of the Royal Astronomical Society](#), 485, 3661
- Gallet F., Bouvier J., 2013, [Astronomy & Astrophysics](#), 556, A36
- Garaud P., 2002, [Monthly Notices of the Royal Astronomical Society](#), 335, 707
- Gehan C., Mosser B., Michel E., Samadi R., Kallinger T., 2018, [Astronomy & Astrophysics](#), 616, A24
- Goldreich P., Schubert G., 1967, [The Astrophysical Journal](#), 150, 571
- Gordon T. A., Davenport J. R. A., Angus R., Foreman-Mackey D., Agol E., Covey K. R., Agüeros M., Kipping D., 2021, arXiv:2101.07886 [astro-ph]
- Gough D. O., Thompson M. J., 1990, [Monthly Notices of the Royal Astronomical Society](#), 242, 25
- Hall O. J., et al., 2021, [Nature Astronomy](#), 5, 707
- Hartman J. D., et al., 2009, [The Astrophysical Journal](#), 691, 342

- Hartman J. D., Bakos G. Á., Kovács G., Noyes R. W., 2010, A Large Sample of Photometric Rotation Periods for FGK Pleiades Stars, doi:10.48550/arXiv.1006.0950, <http://arxiv.org/abs/1006.0950>
- Hatt E., et al., 2023, *Astronomy & Astrophysics*, 669, A67
- Heger A., 1998, PhD thesis, Technical University of Munich
- Heger A., Langer N., Woosley S. E., 2000, *The Astrophysical Journal*, 528, 368
- Henderson C. B., Stassun K. G., 2012, *The Astrophysical Journal*, 747, 51
- Herbst W., Bailer-Jones C. a. L., Mundt R., Meisenheimer K., Wackermann R., 2002, *Astronomy & Astrophysics*, 396, 513
- Hermes J. J., et al., 2017, *The Astrophysical Journal Supplement Series*, 232, 23
- Hollerbach R., Teeluck V., Rudiger G., 2010, *Physical Review Letters*, 104, 044502
- Irwin J., Hodgkin S., Aigrain S., Bouvier J., Hebb L., Moraux E., 2008, *Monthly Notices of the Royal Astronomical Society*, 383, 1588
- Irwin J., Aigrain S., Bouvier J., Hebb L., Hodgkin S., Irwin M., Moraux E., 2009, *Monthly Notices of the Royal Astronomical Society*, 392, 1456
- Johnstone C. P., Güdel M., Brott I., Lüftinger T., 2015a,] 10.1051/0004-6361/201425301
- Johnstone C. P., Güdel M., Lüftinger T., Toth G., Brott I., 2015b, *Astronomy & Astrophysics*, 577, A27
- Kim E.-j., MacGregor K. B., 2000, *AIP Conference Proceedings*, 537, 256
- Kippenhahn R., 1974, in Symposium-International Astronomical Union. Cambridge University Press, pp 20–40
- Kippenhahn R., 1977, *Astronomy and Astrophysics*, 58, 267
- Kippenhahn R., Thomas H.-C., 1970, in International Astronomical Union Colloquium. Cambridge University Press, pp 20–29
- Kippenhahn R., Weigert A., 1990, Stellar Structure and Evolution. <https://ui.adsabs.harvard.edu/abs/1990sse..book.....K>

- Kippenhahn R., Meyer-Hofmeister E., Thomas H. C., 1970, *Astronomy and Astrophysics*, 5, 155
- Lagarde N., Decressin T., Charbonnel C., Eggenberger P., Ekström S., Palacios A., 2012, [Astronomy & Astrophysics](#), 543, A108
- Langer N., 1991, *Astronomy and Astrophysics*, 252, 669
- Lanzafame A. C., Spada F., 2015, [Astronomy and Astrophysics](#), 584, A30
- Li Y., Bedding T. R., Li T., Bi S., Stello D., Zhou Y., White T. R., 2020a, [Monthly Notices of the Royal Astronomical Society](#), 495, 2363
- Li T., Bedding T. R., Christensen-Dalsgaard J., Stello D., Li Y., Keen M. A., 2020b, [Monthly Notices of the Royal Astronomical Society](#), 495, 3431
- Lockwood G. W., Skiff B. A., Henry G. W., Henry S., Radick R. R., Baliunas S. L., Donahue R. A., Soon W., 2007, [The Astrophysical Journal Supplement Series](#), 171, 260
- Lu Y., Curtis J. L., Angus R., David T. J., Hattori S., 2022, [The Astronomical Journal](#), 164, 251
- Maeder A., 1999, *Astronomy and Astrophysics*, 347, 185
- Maeder A., 2003, [Astronomy and Astrophysics](#), 399, 263
- Maeder A., 2009, Physics, Formation and Evolution of Rotating Stars. Springer
- Maeder A., Meynet G., 1997, *Astronomy and Astrophysics*, 321, 465
- Maeder A., Meynet G., 2000, [Annual Review of Astronomy and Astrophysics](#), 38, 143
- Maeder A., Zahn J.-P., 1998, *Astronomy and Astrophysics*, 334, 1000
- Mathis S., Zahn J.-P., 2004, [Astronomy and Astrophysics](#), 425, 229
- Mathis S., Prat V., Amard L., Charbonnel C., Palacios A., 2018, [Astronomy & Astrophysics](#), 620
- Matt S. P., MacGregor K. B., Pinsonneault M. H., Greene T. P., 2012, [The Astrophysical Journal](#), 754, L26

- McQuillan A., Mazeh T., Aigrain S., 2014, [The Astrophysical Journal Supplement Series](#), 211, 24
- Meibom S., Mathieu R. D., Stassun K. G., 2009, [The Astrophysical Journal](#), 695, 679
- Meibom S., et al., 2011, [The Astrophysical Journal](#), 733, L9
- Menou K., Mer J. L., 2006, [The Astrophysical Journal](#), 650, 1208
- Mestel L., 1953, [Monthly Notices of the Royal Astronomical Society](#), 113, 716
- Mestel L., Spitzer Jr. L., 1956, [Monthly Notices of the Royal Astronomical Society](#), 116, 503
- Metcalfe T. S., et al., 2010, [The Astrophysical Journal](#), 723, 1583
- Milne E. A., 1923, [Monthly Notices of the Royal Astronomical Society](#), 83, 118
- Mishra A., Mamatsashvili G., Galindo V., Stefani F., 2021, [Journal of Fluid Mechanics](#), 922, R4
- Montesinos B., Thomas J. H., Ventura P., Mazzitelli I., 2001, [Monthly Notices of the Royal Astronomical Society](#), 326, 877
- Moraux E., et al., 2013, [Astronomy and Astrophysics](#), 560, A13
- Mosser B., et al., 2012, [Astronomy & Astrophysics](#), 548, A10
- Moyano F. D., Eggenberger P., Meynet G., Gehan C., Mosser B., Buldgen G., Salmon S. J. A. J., 2022, [Astronomy & Astrophysics](#), 663, A180
- Noyes R. W., Hartmann L. W., Baliunas S. L., Duncan D. K., Vaughan A. H., 1984, [The Astrophysical Journal](#), 279, 763
- Núñez A., et al., 2022, [The Astrophysical Journal](#), 931, 45
- Ouazzani R.-M., Marques J. P., Goupil M.-J., Christophe S., Antoci V., Salmon S. J. A. J., 2018, arXiv e-prints, 1801, arXiv:1801.09228
- Pantillon F. P., Talon S., Charbonnel C., 2007, [Astronomy & Astrophysics](#), 474, 155
- Parker E. N., 1958, [The Astrophysical Journal](#), 128, 664

- Pinçon C., Belkacem K., Goupil M. J., Marques J. P., 2017, *Astronomy & Astrophysics*, 605, A31
- Pinsonneault M. H., Kawaler S. D., Sofia S., Demarque P., 1989, *The Astrophysical Journal*, 338, 424
- Pizzolato N., Maggio A., Micela G., Sciortino S., Ventura P., 2003, *Astronomy and Astrophysics*, 397, 147
- Reinhold T., Gizon L., 2015, *Astronomy & Astrophysics*, 583, A65
- Reinhold T., Hekker S., 2020, *Astronomy & Astrophysics*, 635, A43
- Reinhold T., Reiners A., 2013, *Astronomy and Astrophysics*, 557, A11
- Reinhold T., Bell K. J., Kuszlewicz J., Hekker S., Shapiro A. I., 2019, *Astronomy & Astrophysics*, 621, A21
- Rüdiger G., Schultz M., Stefani F., Mond M., 2015, *The Astrophysical Journal*, 811, 84
- Ruediger G., Gellert M., Schultz M., Hollerbach R., Stefani F., 2014, *Monthly Notices of the Royal Astronomical Society*, 438, 271
- Santos A. R. G., Breton S. N., Mathur S., García R. A., 2021, *The Astrophysical Journal Supplement Series*, 255, 17
- Schatzman E., 1962, *Annales d'Astrophysique*, 25, 18
- Skumanich A., 1972, *The Astrophysical Journal*, 171, 565
- Soderblom D. R., Stauffer J. R., Hudon J. D., Jones B. F., 1993, *The Astrophysical Journal Supplement Series*, 85, 315
- Spada F., Lanzafame A. C., 2020, *Astronomy & Astrophysics*, 636, A76
- Spada F., Gellert M., Arlt R., Deheuvels S., 2016, *Astronomy & Astrophysics*, 589, A23
- Spina L., et al., 2020, *The Astrophysical Journal*, 895, 52
- Spruit H. C., 1999, *Astronomy and Astrophysics*, 349, 189
- Spruit H. C., 2002, *Astronomy and Astrophysics*, 381, 923
- Spruit H., Phinney E. S., 1998, *Nature*, 393, 139

- Strugarek A., Brun S., Zahn J., 2011, *Astronomy & Astrophysics - ASTRON ASTRO-PHYS*, 532
- Struve O., 1930, *The Astrophysical Journal*, 72, 1
- Struve O., Elvey C. T., 1930, *Nature*, 125, 308
- Sweet P. A., 1950, *Monthly Notices of the Royal Astronomical Society*, 110, 548
- Talon S., Charbonnel C., 2005, *Astronomy & Astrophysics*, 440, 981
- Talon S., Zahn J.-P., 1997, *Astronomy and Astrophysics*, 317, 749
- Tassoul J. L., 1978, Princeton University Press
- Tassoul J.-L., 2000, Stellar Rotation. Cambridge University Press
- Tayar J., et al., 2015, *The Astrophysical Journal*, 807, 82
- Vaughan A. H., Preston G. W., 1980, *Publications of the Astronomical Society of the Pacific*, 92, 385
- Weber E. J., Davis Jr. L., 1967, *The Astrophysical Journal*, 148, 217
- Wright N. J., Drake J. J., Mamajek E. E., Henry G. W., 2011, *The Astrophysical Journal*, 743, 48
- Zahn J.-P., 1974, in Symposium-International Astronomical Union. Cambridge University Press, pp 185–195
- Zahn J. P., 1975, *Memoires of the Societe Royale des Sciences de Liege*, 8, 31
- Zahn J.-P., 1992, *Astronomy and Astrophysics*, 265, 115
- Zhang J., et al., 2020, *The Astrophysical Journal Supplement Series*, 247, 9
- den Hartogh J. W., Eggenberger P., Hirschi R., 2019, *Astronomy & Astrophysics*, 622, A187
- van Saders J. L., Pinsonneault M. H., Barbieri M., 2019, *The Astrophysical Journal*, 872, 128
- von Zeipel H., 1924, *Monthly Notices of the Royal Astronomical Society*, 84, 684